

Key Points:

- Two estimated epicenters of three low-frequency marsquakes are near Cerberus Fossae
- Diverse faulting mechanisms of marsquakes are estimated from single-station relative body wave amplitudes, using a novel misfit definition
- The origins of the analyzed marsquakes may be volcano-tectonic, related to magmatic activity in the lower crust

Correspondence to:

M. Sita,
ms4sc@virginia.edu

Citation:

Sita, M., & van der Lee, S. (2022). Potential volcano-tectonic origins and faulting mechanisms of three low-frequency marsquakes detected by a single InSight seismometer. *Journal of Geophysical Research: Planets*, 127, e2022JE007309. <https://doi.org/10.1029/2022JE007309>

Received 23 MAR 2022
Accepted 11 SEP 2022



Potential Volcano-Tectonic Origins and Faulting Mechanisms of Three Low-Frequency Marsquakes Detected by a Single InSight Seismometer

Madelyn Sita^{1,2} and Suzan van der Lee^{2,3}

¹Department of Chemistry, University of Virginia, Charlottesville, VA, USA, ²CIERA, Northwestern University, Evanston, IL, USA, ³Department of Earth and Planetary Sciences, Northwestern University, Evanston, IL, USA

Abstract Utilizing low-frequency events reported by the Marsquake Service (MQS), we selected waveform data collected from the InSight mission to characterize the origins of three potential marsquakes. S0173a and S0235b were determined to originate near the Cerberus Fossae region. Our calculated backazimuths and epicentral distances were in agreement with those provided by the InSight team. The third event, S0325ab, likely originated southeast of the lander with an epicentral distance of 38.4°, uniquely placing it near the boundary between the Martian highlands and lowlands. We then estimated potential double-couple faulting mechanisms associated with each of the marsquakes using the relative amplitudes and polarities of the *P*, *SH*, and *SV* waves, in a novel method. S0173a and S0173ab can be explained with a composite mechanism that begins as a thrust faulting, followed by an oblique normal-faulting mechanism. Given the low level of seismicity on Mars, it is likely that these events did not occur independently but instead form a doublet resulting from a single origin. Though its weaker, S0325a and S0325ab could also represent a doublet that begins with E-W extension and ends with N-S extension. Our preferred explanation for S0235b is a single faulting mechanism representing vertical dip-slip with a small normal-faulting component. The strike of one fault plane aligns roughly with the exposed faults that represent the Cerberus Fossae. We propose that these diverse faulting mechanisms from different locations represent intra-crustal deformation in the form of volcano-tectonic quakes related to magmatic activity, including possible dike propagation in the lower crust.

Plain Language Summary We investigated the data recorded by the first seismometer successfully installed on the surface of Mars, in order to better understand its geological activity and ways in which it is still changing. We analyzed signals from three prominent marsquakes to infer their epicenters and the type of slip that caused them. By comparing the unique properties of these marsquakes to the mechanisms we see on Earth, we attempted to characterize the ways in which Mars deforms. This project adapted methods used on Earth when seismic data is collected from a single station to tackle the difficult task of working with data from one seismometer on the Martian surface in an unfamiliar noise environment. Using this method, we were able to independently reproduce and provide additional details for the results published by the NASA InSight mission team. We find that seismic activity on Mars is not restricted to a single region and represents various faulting styles, sometimes occurring just a few seconds apart. We hypothesize that the analyzed marsquakes are induced by magmatic activity in the lower crust, near the crust-mantle boundary.

1. Introduction

On 26 November 2018, the mission team for the Interior Exploration using Seismic Investigations, Geodesy and Heat Transport (InSight) successfully installed a very broad-band (VBB) seismometer, among other instruments, on the surface of Mars. This instrument, the Seismic Experiment for Interior Structure (SEIS), is the first seismometer on the surface of Mars capable of detecting seismic waves propagating through the interior of the planet (Banerdt et al., 2020). Using this data, seismologists have gained a better understanding of the current processes shaping the red planet as well as investigated the early formation processes of the rocky planets of our inner solar system (Knapmeyer-Endrun & Kawamura, 2020).

Characteristics of the seismic signals aid in enhancing the current models of the interior structure and contribute to our knowledge of the ongoing evolution of Mars. Mars has no active plate tectonics and cooled rapidly during its formation, thus fixing information about its early formation within (Carr, 1999; Knapmeyer-Endrun & Kawamura, 2020). This is in contrast to Earth, where dynamics related to plate tectonics and a slower cooling

history continue to rejuvenate the planetary interior and surface. Models of the interior have been hypothesized for decades based on reasonable assumptions about the composition, temperature and pressure gradients in the Martian interior (Bertka & Fei, 1998; Dreibus & Wanke, 1985; Okal & Anderson, 1978; Zharkov & Gudkova, 2005).

Globally, the thickness of the Martian crust has been estimated to fall between 24 and 72 km (Knapmeyer-Endrun & Kawamura, 2020; Neumann et al., 2004). In the vicinity of the InSight landing site, the Martian crust has been estimated to be 27–45 km thick from analyses of *P*-to-*S* and *PP*-to-*S* receiver functions and one *S*-to-*P* receiver function (Kim et al., 2021; Knapmeyer-Endrun et al., 2021). The landing site falls within a degraded impact crater in the Martian lowlands, Elysium Planitia, which is about 5 km shallower than the Martian highlands to the south and about 3 km higher in elevation than the average elevation in the lowlands (Neumann et al., 2004; Smith et al., 2003). The crust beneath the Martian highlands is inferred to be thicker than the crust beneath the martian lowlands. Therefore, we expect the crust beneath the landing site to be on the low side of average thickness shown in Knapmeyer-Endrun et al. (2021) and Knapmeyer et al. (2006), which is consistent with the 27–45 km estimate of Kim et al. (2021). For comparison, Earth's crust is known to be 6–10 km thick under oceans and 30–70 km under continents.

Earth's lithosphere, including the crust, is subdivided into about a dozen tectonic plates that move atop a viscous, mostly solid mantle due to convection currents. Conversely, the lithosphere of Mars is not subdivided into individual tectonic plates and is postulated to have well defined layers due to a lack of convection (Carr, 1999; Lognonné et al., 2019). The density, rigidity, and incompressibility of these layers, which change with composition, constitution, temperature, and pressure, determine how seismic waves propagate through the interior of Mars. Therefore, seismic waves can be used as a tool to map these layers as well as draw inferences about early planetary formation processes (Knapmeyer-Endrun & Kawamura, 2020; Lognonné et al., 2019). In order to study the interior structure of Mars, knowledge of the origin times, locations, and characteristics of these seismic events is needed. In this paper, we studied features of individual marsquake events, specifically the ones that generated significant low-frequency signals that are thought to have traversed the mantle and crust of Mars (Khan et al., 2021).

Without seismically active boundaries between individual tectonic plates, intraplate tectonics and meteorite impacts were expected to be the major contributors to the seismicity of Mars (Clinton et al., 2018; Lognonné et al., 2019). The InSight lander is located about 1,600 km west of Cerberus Fossae, which was hypothesized to be an active tectonic structure based on evidence of faulting in pre-mission orbital images (Banerdt et al., 2020; Taylor et al., 2013). Shortly after the onset of this study, Giardini et al. (2020) located epicenters of two marsquakes with the clearest low-frequency signals recorded by InSight during year one, S0173a and S0235b, near Cerberus Fossae.

For this study, we explored the 465 marsquake-type events detected and reported by the Marsquake Service (MQS) in Version 2 of the Mars Seismic Catalog and identified the strongest candidates for representing signals from Earth-like quakes, that is, shear dislocation on a fault plane, hereafter called marsquakes. We investigated the events categorized as either low frequency, which is defined as events where all three components show energy below 2.4 Hz, or broadband for features that indicated marsquake origins for the events. This included examinations of the signal in different frequency bands and over the three components for signatures of *P* and *S* wave energy in the particle motion of the possible wave's arrival time window. We confirmed that events S0173a and S0235b had the most prominent marsquake signatures and their waveforms were used as reference for selecting and analyzing additional events within the MQS catalog.

The project focused on these low frequency and broadband events as they were the most likely to have body waves which traveled through both the mantle and crust of the planet (Giardini et al., 2020). Body waves include primary waves, or *P*-waves, which are longitudinal, and secondary waves, or *S*-waves, which are transverse. The *P*-waves cause particle motion back and forth along the direction of wave propagation and tracing that motion can be used to estimate the direction to the epicenter relative to the lander. *SV*-waves are *S*-waves with particle motion that is, like *P*-waves, within the vertical plane through the lander and epicenter, and, unlike *P*-waves, perpendicular to the direction of wave propagation. *SH*-waves are *S*-waves with horizontal particle motion perpendicular to the vertical plane through the lander and epicenter, and thus perpendicular to the direction of wave propagation. *S*-waves propagate slower than *P*-waves, so the delay in arrival time at the seismometer can be used to estimate

Table 1
This Table Presents the Azimuth and Dip Angles of Seismometer Components

	Azimuth (°)	Dip (°)
<i>U</i>	135.1	-29.4
<i>V</i>	15	-29.2
<i>W</i>	255	-29.7

the epicentral distance (Gutenberg & Richter, 1941). Considering the relative amplitudes of the three types of body waves can also provide clues about the type of faulting associated with a marsquake (Langston, 1979). We calculated the epicenters of the two reference events, S0173a and S0235b, as described in the Methods section, and verified them against the epicenters reported by the InSight mission team (Brinkman et al., 2021; InSight Marsquake Service, 2021). We then selected an additional event, S0325a, and calculated its epicenter using the same method. Additionally, we explored the origins associated with these seismic signals by measuring and analyzing the relative amplitudes and polarities of the recorded *P*- and *S*-waves and assessing the possible faulting mechanisms.

2. Methods

2.1. Locating the Marsquakes

The InSight SEIS waveform data were downloaded directly from the Incorporated Research Institutions for Seismology (IRIS) database (InSight Mars SEIS Data Service, 2019) for each of the events using a function of the Python package ObsPy (Krischer et al., 2015). The instrument of interest for this project is the VBB seismometer, characterized by network name XB and station name ELYSE. We accessed the 20 samples per second data stream by using sensor location code 02, and raw, broad-band, high dynamic range sensor components BHU, BHV, and BHW. The seismogram for each component was converted to ground displacement via deconvolution with the component's response function. The raw data streams from the components, labeled *U*, *V*, and *W*, were then recombined to reflect ground motion in the north, east, and vertical directions, using information provided by Suemoto et al. (2020) on the orientation of the seismometer on the planet's surface as well as the components within the instrument.

Using Equation 1 from Supporting Information S1 of Suemoto et al. (2020) we rotated the data streams $u(t)$ as follows.

$$\begin{pmatrix} u_E(t) \\ u_N(t) \\ u_Z(t) \end{pmatrix} = \begin{pmatrix} \cos(\varphi_U) \sin(\theta_U) & \cos(\varphi_U) \cos(\theta_U) & -\sin(\varphi_U) \\ \cos(\varphi_V) \sin(\theta_V) & \cos(\varphi_V) \cos(\theta_V) & -\sin(\varphi_V) \\ \cos(\varphi_W) \sin(\theta_W) & \cos(\varphi_W) \cos(\theta_W) & -\sin(\varphi_W) \end{pmatrix}^{-1} \begin{pmatrix} u_U(t) \\ u_V(t) \\ u_W(t) \end{pmatrix} \quad (1)$$

where $u_i(t)$ represents ground displacement for component i as a function of time t , φ_i represents the dip angle of component i , and θ represents the azimuth of component i . The values used for φ and θ are listed in Table 1, as documented in Suemoto et al. (2020).

Next, both the raw and the rotated data was filtered over different frequency ranges to visually inspect the wave-trains, confirm the identification of the *P*- and *S*-wave energy, and take note of glitches that would affect our analyses. Data selected for further analysis and presented below was uniformly bandpass-filtered between 0.125 and 1 Hz for all events.

The three rotated and perpendicular components were used to plot the particle motion of the arriving body waves. These results were used to confirm the energy resembled *P*- and *S*-waves as well as estimate back azimuth (direction) from which the event originated. Using our calculated difference in arrival time between the two body wave arrivals and an estimated source depth of 35 km, we approximated the horizontal distance to the epicenter using travel time plots created by the TauP toolkit (Buland & Chapman, 1983; Crotwell et al., 1999). This depth was chosen because the incidence angles derived from the particle motion plots aligned, within uncertainties, with those calculated from our favored interior structure models at 35 km depth. Our investigation showed that changing the depth by 20 km would typically result in the epicentral distance changing by less than one degree. However, all depths modeled had calculated incidence angles within the uncertainties, making it difficult to constrain the depth from the observed incidence angle.

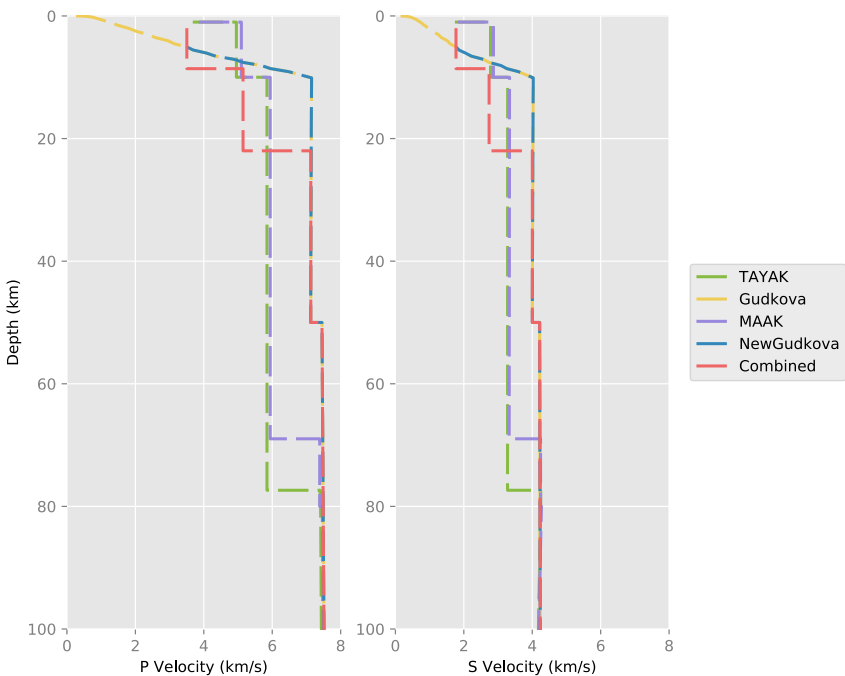


Figure 1. The P and S velocity over the top 100 km of the Gudkova, MAAK and TAYAK Martian interior structure models as published in Clinton et al. (2017). The New Gudkova model above was derived using observations from the InSight data and from the original pre-mission Gudkova model (Zharkov & Gudkova, 2005). The Combined model presented above is an adapted version of the New Gudkova model and the model presented in Knapmeyer-Endrun et al. (2021).

We selected our favored interior structure model by analyzing 13 previously published velocity models based on pre-mission estimates of the Martian interior from Clinton et al. (2017) in addition to two models adapted from Zharkov and Gudkova (2005) and Knapmeyer-Endrun et al. (2021), which used InSight data to inform the published structure model. The models varied in their estimations of the core depth, ranging from 1,539 to 1,870 km, as well as the Moho depth, which ranged from 32 to 90 km. Only three models, Gudkova, MAAK, and TAYAK, in addition the New Gudkova and the Combined model presented in this paper, could recreate the differential travel times calculated for our events (Khan et al., 2016; Zharkov & Gudkova, 2005). These models are shown in Figure 1. The remaining 10 models from Clinton et al. (2017) had low velocity zones which produced a S -wave shadow zone that included our measured travel time differences for one or more events. Further analysis revealed the Gudkova model was most consistent with the observations of different event parameters. This model, however, included multiple shallow velocity changes due to thin layers of unconsolidated regolith, sand, and dust on the surface that produced extremely steep incident angles not seen in our observations. Therefore, the New Gudkova model was created by removing these shallow boundaries completely and was used as the preferred model throughout the remainder of this study. In July 2021, over a year after the onset of our study, the first models of the Martian interior structure using InSight observations were published by Knapmeyer-Endrun et al. (2021). Their proposed structure included a thicker crust than our preferred New Gudkova model in addition to lower body wave velocities within the crust and a discontinuity between 20 and 25 km. By combining the average model parameters presented by Knapmeyer-Endrun et al. (2021) with the New Gudkova model, the Combined model presented in Figure 1 was created. Results from this model were largely consistent with earlier results from the preferred pre-mission models and fell within our uncertainty estimates, indicating that our conclusions are not strongly model dependent. We illustrate this in Appendix A.

Once the epicentral distance was estimated, we calculated the back azimuth by determining the angle at which the energy on the transverse component of the seismogram was minimal at the time of the P -wave arrival, using the methods presented by Olugboji (2020) (Braunmiller et al., 2020; Dannemann Dugick et al., 2021; Ojo et al., 2019).

For all three marsquakes, the epicentral distances (estimated from $S-P$ arrival time differences) and the back azimuths (estimated from rotating the horizontal components until P energy was minimized on one horizontal

component) were cross referenced with particle motion plots and found to be consistent with estimates of observed incidence angles and back azimuths.

2.2. Estimating the Faulting Mechanism

We modeled waveform amplitudes for a range of possible double couple faulting mechanisms to compare to the observed P , SH , and SV waveform amplitudes. In the absence of sufficiently accurate knowledge of the marsquakes' seismic moment and the density, geometrical spreading, layer-boundary, and attenuative properties of the Martian interior, we modeled relative rather than absolute amplitudes of the direct P and S body waves. Relative P , SV and SH body wave amplitudes, A^P , A^{SV} , and A^{SH} , respectively, were modeled using expressions for far-field body waves (Aki & Richards, 1980; Stein & Wysession, 2009). After converting to the vertical-radial-transverse coordinate system conventionally used in observational seismology, the expressions are:

$$\begin{aligned} A^P(\phi, i) &\sim (s_R(3\cos^2(i) - 1) - q_R\sin(2i) - p_R\sin^2(i)) / \alpha^3 \\ A^{SV}(\phi, j) &\sim (1.5s_R\sin(2j) + q_R\cos(2j) + 0.5p_R\sin(2j)) / \beta^3 \\ A^{SH}(\phi, j) &\sim (q_L\cos(j) + p_L\sin(j)) / \beta^3 \end{aligned} \quad (2)$$

where

$$\begin{aligned} s_R &= \sin(\lambda)\sin(\delta)\cos(\delta) \\ q_R &= \sin(\lambda)\cos(2\delta)\sin(\psi - \phi) + \cos(\lambda)\cos(\delta)\cos(\psi - \phi) \\ p_R &= \cos(\lambda)\sin(\delta)\sin(2(\psi - \phi)) - \sin(\lambda)\sin(\delta)\cos(\delta)\cos(2(\psi - \phi)) \end{aligned} \quad (3)$$

and

$$\begin{aligned} p_L &= \sin(\lambda)\sin(\delta)\cos(\delta)\sin(2(\psi - \phi)) + \cos(\lambda)\sin(\delta)\cos(2(\psi - \phi)) \\ q_L &= -\cos(\lambda)\cos(\delta)\sin(\psi - \phi) + \sin(\lambda)\cos(2\delta)\cos(\psi - \phi) \end{aligned} \quad (4)$$

where ϕ is the ray paths' azimuth, i is the P -wave exit angle (take-off angle), j is the S -wave exit angle, ψ is the fault strike, δ is the fault dip, λ is the slip rake, α is the P -velocity at the source depth, and β is the S -velocity at the source depth.

The exit and incidence angles of the body waves were calculated using the TauP toolkit (Buland & Chapman, 1983; Crotwell et al., 1999) and based on the velocity model as well as the estimated epicentral distance of the event. The azimuths used for the modeled amplitudes are based on the estimated epicenters of the events and the location of the seismometer.

To measure the amplitude of body waves in the direction in which they are polarized, we first rotated the horizontal north and east components of the seismogram to the also horizontal radial and transverse components. For reference, the radial component points from the seismometer into the opposite direction of the epicenter and the transverse component points in a horizontal direction rotated 90° clockwise from the radial component. If one considers a cross-sectional vertical plane through the epicenter and station, then the radial component is the horizontal component along the length of the cross section and the transverse component is perpendicular to the cross-sectional plane. The vertical component points upwards.

In a laterally homogeneous planet, P -waves will produce energy on only the vertical and radial components, not on the transverse component. S -waves, on the other hand, will produce energy on both the radial as well as the transverse component. The S -waves predominantly recorded on the radial component are called SV -waves while those predominantly recorded on the transverse component are called SH -waves. Next, and within this vertical plane, we rotated the vertical and radial components by i_o , the P incidence angle at the seismometer, such that the L component of the resulting L and Q components aligns with the direction of P -wave propagation. We then measured the P amplitude on this L component. The vertical and radial components were rotated in the same sense by j_o , the SV incidence angle at the seismometer, such that the Q component of the resulting L and Q components aligns with the polarization of the incident SV wave and the horizontal component of the Q component

continues to point in the radial direction. The *SV* amplitude was measured on this *Q* component. *SH* amplitudes were measured on the transverse component, *T*.

Because of the relatively high quality of the low-frequency event signals, we were able to adapt, combine, and apply established methods of fault plane determination based on first-motion polarities and amplitude ratios of *P*, *SV*, and *SH* body waves recorded by a single seismometer (Ebel & Bonjer, 1990; Langston, 1979; Schwartz, 1995). Shang and Tkalcic (2020) take first-motion polarities and amplitude ratios into account as separate observations and show that this can lead to better-constrained, more complex source mechanisms compared to methods that take only polarities or amplitude ratios into account. Hardebeck and Shearer (2003) point out that using body wave amplitude ratios alone can allow noise to have outsized effects, especially if body waves leave the source near a nodal plane in the radiation pattern. Our method takes relative amplitudes and the signs of the amplitudes (first-motion polarities) into account simultaneously, and is less sensitive to nodal-plane radiation by not explicitly using amplitude ratios.

Using the measured amplitudes of the observed direct *P*, *SH*, and *SV* waves on the *L*, *T*, and *Q* components, respectively, we performed a grid search across a range of possible double-couple faulting mechanisms to find acceptable solutions and determine the best fitting solution. This grid search was performed over a tightly gridded range of strike, dip and rake values varying by 2° on each pass in addition to varying the depth from 15 to 55 km by 10 km. While fitting the observations, we upweighted the *P* amplitude and its estimated error by a factor of 5 to counteract its relatively small effect on the misfit resulting from the division by α^3 in Equation 2. Each mechanism was tested in each set of parameters to produce synthetic amplitudes which were compared to the observed amplitudes using our misfit function defined in Equation 5.

The misfit function treated the individual and signed *P*, *SV*, and *SH* amplitude values of the observations, as well as the amplitudes produced by the synthetic fault planes, as components of three-dimensional vectors. We defined the misfit value as the angle between the two vectors, which was calculated in three-dimensional amplitude space for each synthetic faulting mechanism to determine how closely it predicted the observed relative amplitudes. Through this method, the signs of the amplitudes were preserved, zero-valued amplitudes were accommodated, and the resulting misfits calculated were stable over the entire amplitude domain investigated. In other words, this approach avoids the pitfalls of working with ratios. The angle ζ between the observed and synthetic amplitude vectors, \vec{A}_o and \vec{A}_s respectively, was obtained from their inner product as follows:

$$\zeta = \arccos \left(\frac{\vec{A}_o \cdot \vec{A}_s}{\|\vec{A}_o\| \|\vec{A}_s\|} \right), \quad (5)$$

where $\vec{A} = (A^P, A^{SV}, A^{SH})^T$, that is, a vector containing the amplitudes of seismic phases *P*, *SV*, and *SH*. We define the unit vector $\hat{A} = \vec{A}/\|\vec{A}\|$, for use below.

We successfully tested this method of estimating a double-couple faulting mechanism from *P* and *S* displacement waveform amplitudes on the shallow M6.2 earthquake near Naalehu, Hawaii on 10 October 2021. Results of this test are in Appendix D.

Estimated observational errors, σ^P , σ^{SV} , and σ^{SH} , in the measured amplitudes form a trivariate Gaussian distribution around \vec{A}_o , the contours of which outline confidence ellipsoids. We define the following three error vectors from these estimated uncertainties, $\vec{\sigma}^P = (\sigma^P, 0, 0)^T$, $\vec{\sigma}^{SV} = (0, \sigma^{SV}, 0)^T$, and $\vec{\sigma}^{SH} = (0, 0, \sigma^{SH})^T$. Given that our method compares relative amplitudes, the components of the error vectors that are parallel to \vec{A}_o do not contribute to detectable uncertainty. Using only the error vector components within a plane orthogonal to \vec{A}_o , we approximate the error ellipse in this plane as a circle with radius e , where

$$e = \sqrt{\|\vec{\sigma}_\perp^P\|^2 + \|\vec{\sigma}_\perp^{SV}\|^2 + \|\vec{\sigma}_\perp^{SH}\|^2}, \quad (6)$$

Table 2*Table Summarizing the Event Parameters Used in Our Analysis*

Source parameters	S0173a	S0173ab	S0235b	S0325a	S0325ab
Back-azimuth (°)	90	86	72	123	139
Epicentral distance (°)	28.4	28.4	27.3	38.3	38.4
Epicenter	3.95°N 164.09°E	5.86°N 164.11°E	11.22°N 162.04°E	-23.94°N 162.102°E	-23.94°N 162.10°E
Origin Date	2019-05-23	2019-05-23	2019-07-26	2019-10-26	2019-10-26
Origin Time (UTC)	02:19	02:19	12:16	06:54	06:54
P-wave arrival time (UTC)	02:22:59.48	02:23:03.30	12:19:18.70	06:58:58.0	06:59:08.23
S-wave arrival time (UTC)	02:25:53.27	02:25:56.9	12:22:05.7	07:02:49.3	07:02:59.9

Note. The arrival times listed are the times we choose as the first arrivals. Using these times an arrival time difference was determined and used to calculate the epicentral distance using the New Gudkova model and a depth of 35 km.

and

$$\begin{aligned}\vec{\sigma}_{\perp}^P &= \vec{\sigma}^P - (\vec{\sigma}^P \cdot \hat{A}_o) \hat{A}_o, \\ \vec{\sigma}_{\perp}^{SV} &= \vec{\sigma}^{SV} - (\vec{\sigma}^{SV} \cdot \hat{A}_o) \hat{A}_o, \\ \vec{\sigma}_{\perp}^{SH} &= \vec{\sigma}^{SH} - (\vec{\sigma}^{SH} \cdot \hat{A}_o) \hat{A}_o.\end{aligned}\quad (7)$$

Finally, we use the radius of the approximate error circle to estimate an angle of tolerance ϵ , which outlines a cone around \hat{A}_o .

$$\epsilon = \arctan \left(\frac{e}{\|A_o\|} \right) \quad (8)$$

Every \vec{A}_s that makes an angle ζ with \vec{A}_o that is smaller than the tolerance angle ϵ (*i.e.*, falls within the cone) is considered an acceptable fit for the measured amplitudes. However, we do favor the predicted amplitude vector \vec{A}_s that produces the smallest misfit ζ with the vector of observed amplitudes, \vec{A}_o .

3. Results

We analyzed three high-quality marsquake events labeled S0173a, S0235b, and S0325ab listed in Table 2. We used results from the InSight team's previous analysis of the first two events in (Brinkman et al., 2021), as references for validating our analysis methods. Our analysis includes event hypocenters and double-couple faulting mechanisms, as well as estimates of the uncertainties surrounding the presented solutions.

Event parameters used for our analysis are listed in Table 2 and their epicentral areas are shown in Figure 2 superimposed upon Mars' topography from Smith et al. (2003). S0173a and S0235b occurred to the east of the lander with radial distances of 28.4° and 27.3° respectively and falling within an area containing the Cerberus Fossae. These results are consistent with those determined by the InSight team (Brinkman et al., 2021; Zenhäusern et al., 2022). The third event, S0325ab, was weaker and thus harder to locate. Our analysis shows that S0325ab likely occurred to the south-east of the lander with a radial distance of 38.4°, uniquely placing it near the boundary between the Martian highlands in the south and the lowlands in the north. Event S0325ab was preceded by an even weaker event, S0325a, with a more ambiguous epicenter due to a low-signal to noise ratio. One possibility for S0325a's epicenter is south-east of the lander, near the epicenter of S0325ab. The other possible epicenter is north-east of the lander and is the preferred location for S0325a presented by Zenhäusern et al. (2022). Both possibilities are presented in Figure 2.

After the initial *P* and *S* arrivals, InSight Marsquake Service (2021) indicates a second arrival of *P* and *S* waveforms in the seismograms from S0173a and S0325a. Upon inspection, we found that these secondary arrivals did not agree with predicted *pP*, *sP*, *pS* or *sS* arrival times by the published seismic-velocity models. The second *P* arrival had similar particle motion as the initial *P* arrival albeit with a slightly different horizontal polarization, indicating an associated, modest shift in back azimuth for the second events (Figures 3a and 3b).

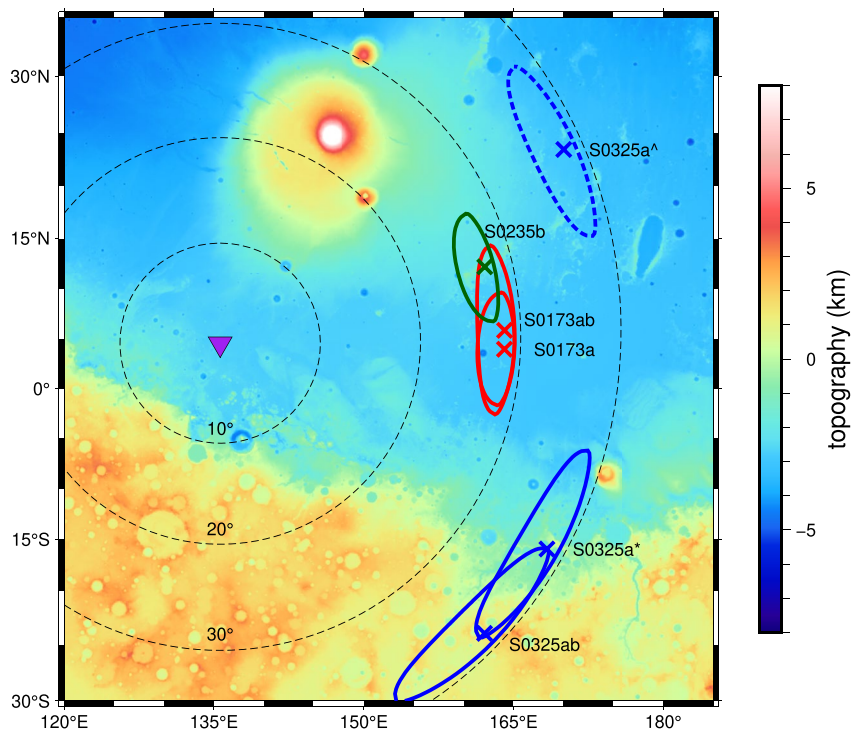


Figure 2. Estimated epicentral locations, marked by X, for each event superimposed on Mars Orbiting Laser Altimeter (MOLA) shaded relief as presented in Smith et al. (2003). Colored lines around the X symbols outline regions of estimated uncertainty for each event. The location of the InSight lander (purple triangle) is shown with respect to the four events discussed: S0173a (3.95°N and 164.09°E) in red, S0173ab (5.86°N and 164.11°E) in red, S0235b (11.22°N and 162.04°E) in green, S0325a* (-23.94°N , 162.10°E) in blue, and S0325ab (-23.94°N and 162.10°E) in blue. S0325a* is our preferred location for the event however we show a second possible location, S0325a[†].

For S0173a, the second *P*-like arrival occurred about 4 s after the initial one and indicated a shift in the epicenter about 4° toward the north, which falls within the confidence region for S0173a's epicenter (Figure 2). The second *S*-like arrival also arrived about 4 s after the first. A hypocenter and origin time for the second pair of body wave arrivals was also determined and the event was labeled S0173ab and listed in Table 2.

For S0325a, the second *P*- and *S*-like arrivals occurred nearly 11 s after the initial ones and with higher *S* amplitudes than the first (Figure 3d). We associated the second arrivals with a distinct marsquake at a similar distance as S0325a and labeled the second event S0325ab. The low-amplitude arrivals associated with S0325a allow for two distinct back azimuths: One similar to and within uncertainties of the S0325ab back azimuth toward the south-east from the lander, and the other pointing north-east from the lander, in the direction of where Zenhäusern et al. (2022) estimated its epicenter.

3.1. S0173a and S0173ab

Events S0173a and S0173ab were analyzed as discrete events, about four seconds apart, with measurable *P* and *S* amplitudes (Figure 4). Both were found to be located within the Cerberus Fossae region between a distance of 28° and 29° and with slightly different back azimuths (Figure 2). Each event produced a unique faulting mechanism solution shown in Figure 5. Because of their proximity in epicenter locations and arrival times, this doublet event likely consisted of two subevents with different mechanisms 4 s apart.

Our grid search for S0173a found a range of mechanisms that fit the measured amplitudes within the tolerance level determined by the pre-arrival noise. This group of mechanisms is dominated by thrust faults with relatively N-S striking fault planes (Appendix C). The best-fitting mechanism is shown in Figure 5. For event S0173ab, the best-fitting mechanism is strike-slip, but the complete solution set appears to favor normal faulting. If the S0173ab mechanism is normal faulting, then this implies a mechanism reversal of E-W compression, for S0173a,

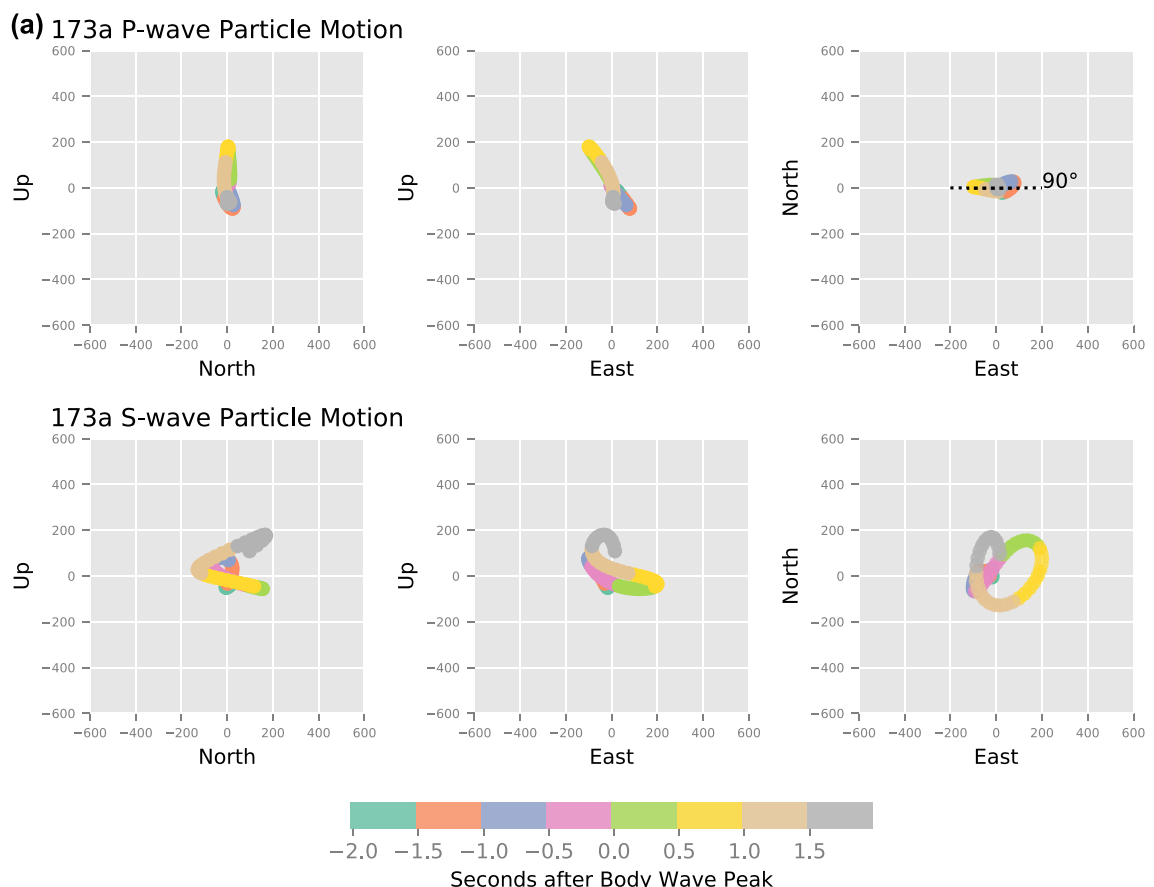


Figure 3. The three particle motion cross sections of *P*-wave and *S*-wave arrival times for each event are shown. Each color represents 0.5 s of data.

followed by E-W tension, for S0173ab. If the S0173ab mechanism is transform faulting, then the *T* axes of all acceptable strike-slip mechanisms are relatively similar. The *N* and *P* axes seem to rotate around a relatively stable, median *T* axis that is roughly oriented WSW-ENE.

Neither of these mechanisms were in agreement with the almost vertical dip slip mechanism that was the proposed solution by InSight as presented in Brinkman et al. (2021). Treating our proposed solutions as components of a composite mechanism, however, can successfully recreate the previously published results (see Section 4 below).

3.2. S0235b

The *S*-labeled phase for S0235b has *SH* and *SV* waves that do not begin at the same time and start to align around 167 s after the *P*-wave arrival, where we measured their amplitudes. *S* energy on the *T* component before that time is similar to the preceding noise and unconvincing as an *SH* arrival, while the *S* energy preceding the *SV* amplitude pick is considerable and of opposite sign to the *SV* amplitude (Figure 6). As suggested by Knapmeyer-Endrun et al. (2021); Kim et al. (2021), this precursor could be a *P*-wave generated by the *SV*-wave encountering a layer interface at depth *d* in or at the bottom of the crust or both. Using an *S*-wave ray parameter of 0.17 s/km, along with *P* and *S* velocities of 3.5 and 2 km/s, respectively, for the uppermost crustal layer in the Combined model would produce a *Sdp* wave arriving around 2.3 s earlier with up to 30% the amplitude of the incident *S*-wave. However, an *Sdp* wave with this amplitude is not evident on the *L* component, increasing uncertainty around the deduced mechanism for S0235b.

Using the *P*- and *S*-wave arrival times in Table 2, while ignoring the possible *S* to *P* converted arrival on the *Q* component, our measured amplitudes best agree with a near vertical dip-slip faulting mechanism (Figure 7). The strike of the vertical fault plane is roughly aligned with the trends of Cerberus Fossae. Another solution that fits the observed amplitudes almost as well is a reverse faulting mechanism with a north-west oriented *P*

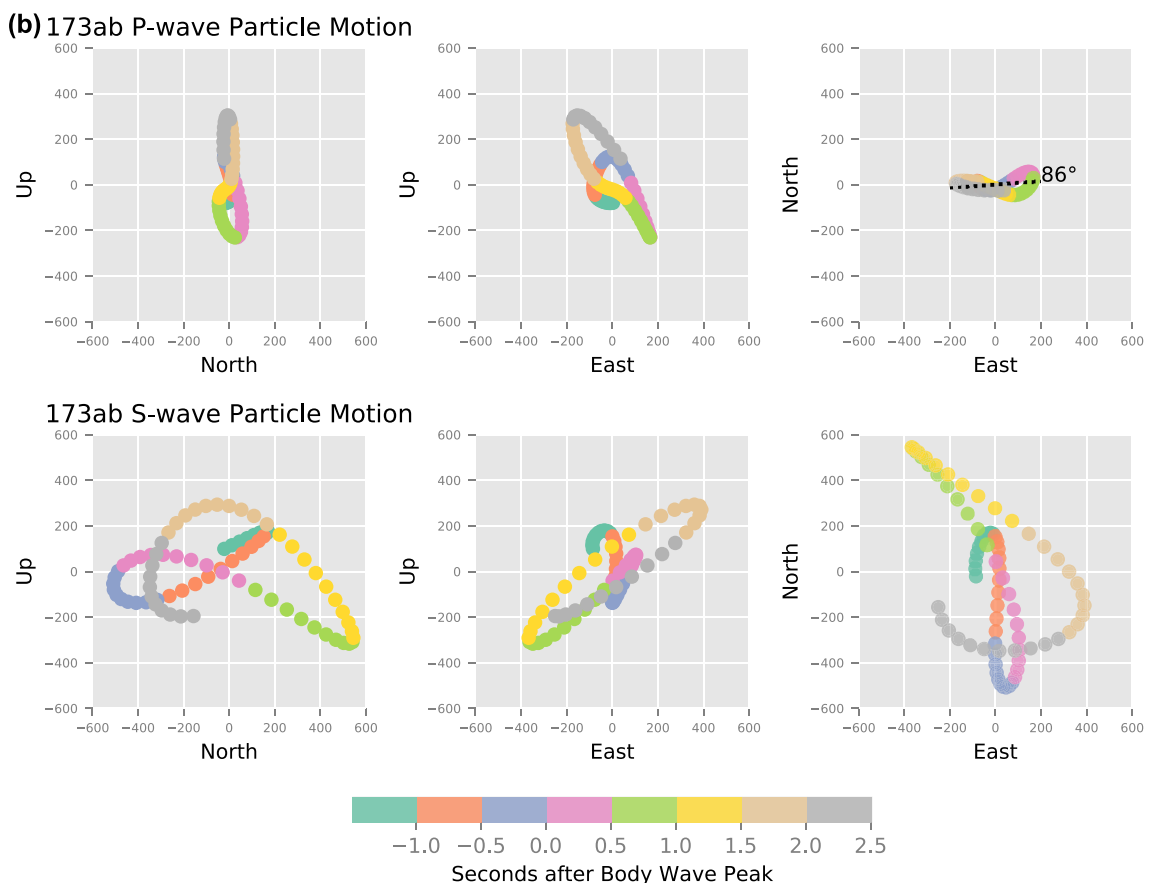


Figure 3. (Continued)

axis. Appendix A shows that this mechanism can become the best-fitting one for different hypocentral depths or seismic-velocity models. However, the complete solution set of all possible mechanisms remains stable with respect to change in hypocentral depth or seismic-velocity model. Both mechanisms differ from the mechanisms proposed by the InSight team. Brinkman et al. (2021) shows a normal faulting mechanism and is possibly influenced by later parts of the waveforms than where we measured our amplitudes.

If we pick the SV amplitude 2.37 s earlier than where we measured its amplitude, it aligns with a zero SH amplitude. Together with the P wave amplitude this produces a best-fitting faulting mechanism that would represent a strike-slip fault.

3.3. S0325ab

There is considerably more uncertainty with the observed amplitudes for S0325ab and thus with the inferred mechanisms. This is because of difficulties in picking the waveforms due to the P -and S -wave signals being close to the noise level and the SH amplitude is small and out of phase with the SV amplitude (Figure 8). Therefore, we chose to set the SH amplitude to 0 ± 0.425 nm. A small local maximum in the T component waveform precedes the timing of the SV amplitude pick and a local minimum succeeds it, but both choices produce solutions that are similar to our presented solution in Figure 9. The relatively low signal to noise ratio for S0325ab and the ambiguous SH arrival produce a large group of mechanisms with misfits within the tolerance determined by pre-arrival noise levels as shown in Appendix C. Because of the even lower signal to noise ratio for S0325a and its multiple possible epicenters, we initially did not attempt to find a faulting mechanism for this event, though we speculate about it in Appendix B. For the second event in this doublet, S0325ab, the best fitting mechanism at a hypocentral depth of 35 km is represented by normal faulting with a roughly N-S oriented T axis, a minor strike-slip component, and one fault plane slightly steeper than the other (Figure 9).

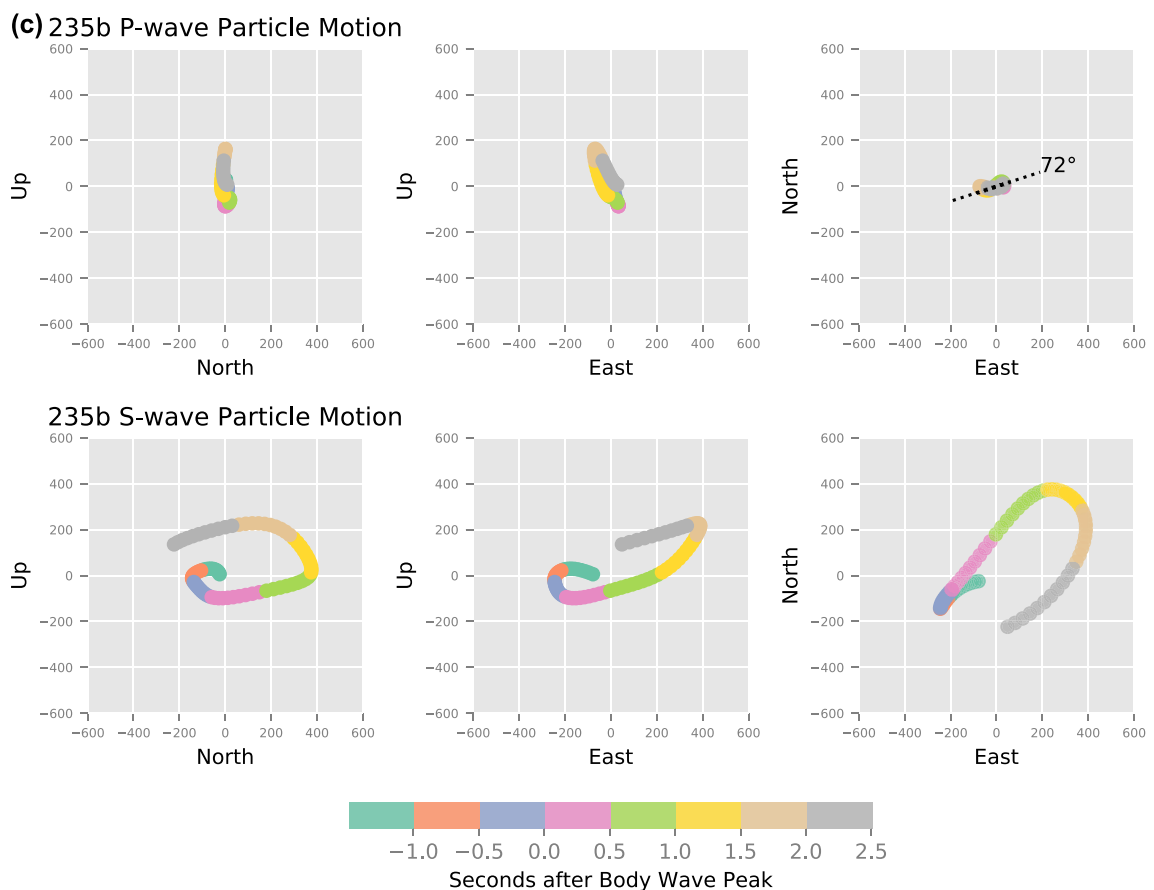


Figure 3. (Continued)

4. Discussion

In the data from InSight spanning 1 January 2019–12 December 2019, we found three plausible marsquakes defined by their measurable P - and S -wave amplitudes. Our investigation of the remaining events reported by InSight Marsquake Service (2020) during that time were either unconvincing or did not have compelling P - and S -wave arrivals necessary for our methods. For example, S0183a, another marsquake analyzed by Brinkman et al. (2021), was marked by convincing P -wave energy arriving on 3 June 2019 02:27:45 UTC. However, the S -wave arrival was marked by a very weak signal possibly due to a S -wave low velocity zone in or beneath the lithosphere (Brinkman et al., 2021; Giardini et al., 2020; Smrekar et al., 2018). The other weaker signals reported by MQS may have also been caused by smaller or farther marsquakes, by volcanic tremor (Kedar et al., 2021), or by environmental events.

Our single-station relative body-wave amplitude method for determining faulting mechanisms was tested on a recent earthquake with a known faulting mechanism, as described in Appendix D. The result of this test suggests that our method can be successfully applied to seismic data from the InSight lander on Mars and potentially other seismically active planetary bodies. The robustness of the presented faulting mechanism estimation method is a result of the definition of misfit, which is based on relative P and S amplitudes and does not have ambiguities with respect to the sign of these amplitudes or become unstable when one or more of the amplitudes vanish. Classical definitions, such as a least-squares estimate of the sum of differences in computed and observed amplitude ratios, become unstable when one of the amplitudes approaches zero. Other possible misfit definitions, for example, the shortest geometrical distance in 3-D amplitude space between the point representing observed amplitudes (for P , SV , and SH arrivals) and the line that represents computed amplitude ratios, do not preserve the signs of the observed amplitudes. Our misfit definition, the angle in 3-D amplitude space between the vector of observed amplitudes and the line of computed amplitudes, is stable over the entire domain and preserves polarity

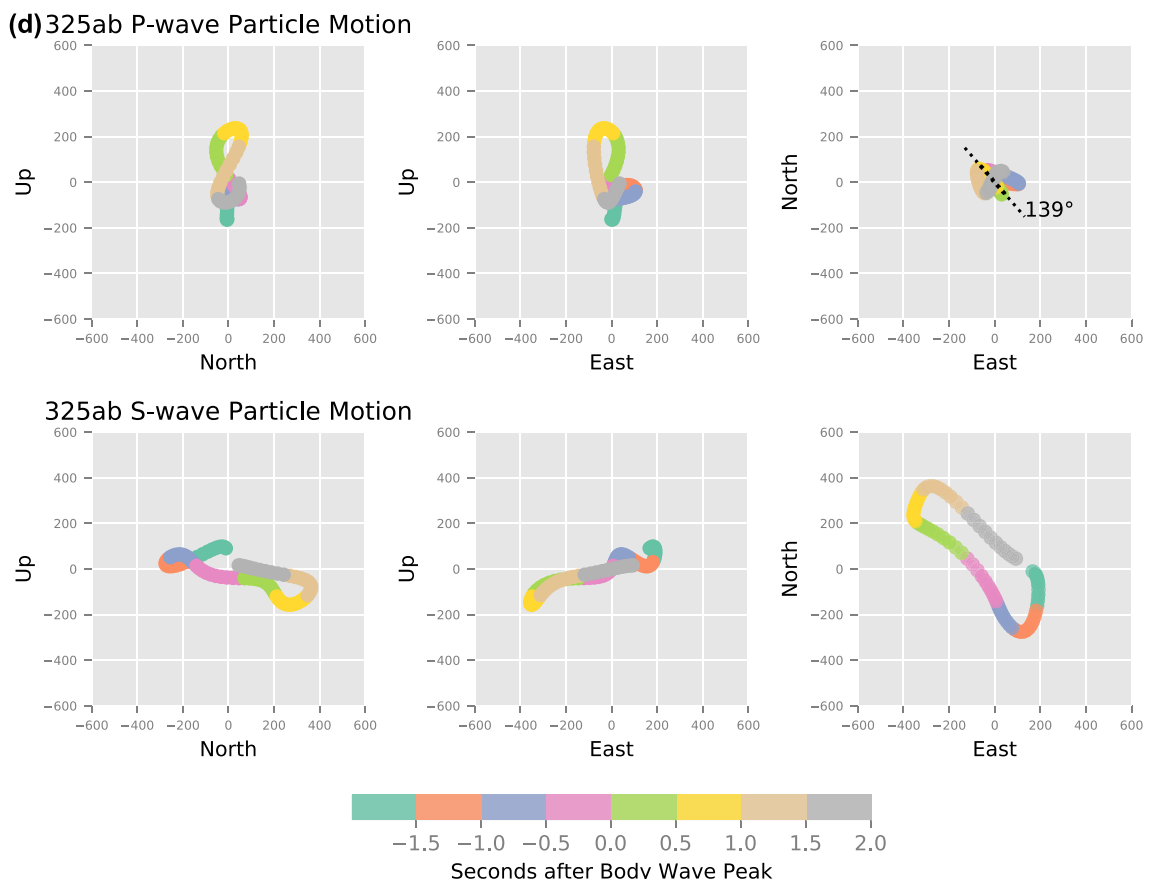


Figure 3. (Continued)

information in the amplitudes, making it a robust and widely applicable misfit definition. Even so, error estimates are large and a number of assumptions needed to be made due to the exploratory nature of this study, facilitated by the first marsquake data recorded.

When measuring the *P*- and *S*-wave displacement amplitudes, the noise levels in the waveforms were reasonably high. This resulted in many possible double-couple faulting solutions for each marsquake due to the relatively high misfit tolerance determined by the pre-arrival noise level in the seismograms. However, one double-couple solution was produced for each marsquake that matched the observed relative amplitudes better than the others, and this is the preferred mechanism presented here. Other acceptable mechanisms are provided in Appendix C and were superimposed into a single beachball figure shown alongside the preferred (best-fitting) mechanisms for each marsquake (Figures 5, 7 and 9).

While describing the characteristics and source mechanisms above, a major assumption was made that all the events included had originated from a point source and were due to a purely double-couple faulting mechanism. In other words, our grid search did not include explosive components or compensated linear vector dipoles, CLVD, in the source mechanisms. Doublet-events S0173a and S0325ab showed the most ambiguity as to whether this was a valid assumption. The arrival times shown in Table 2 were chosen as the strongest candidates for *P* and *S* wave arrivals in the double-event type situation where two sets of potential body waves arrived in close succession. The relative arrival times of these *P*, *SV*, and *SH*, respectively, are the same and that is not possible if the secondary arrivals are reflected seismic phase arrivals, such as so-called depth phases. Thus, we considered the possibility of a mechanism that started with one type of shear dislocation and was followed by a different one at the same or nearby location.

Specifically with S0173a, the InSight team predicted an almost vertical dip slip mechanism in Brinkman et al. (2021) which did not agree with our grid-search solution for either set of arrivals. Figure 4 shows that

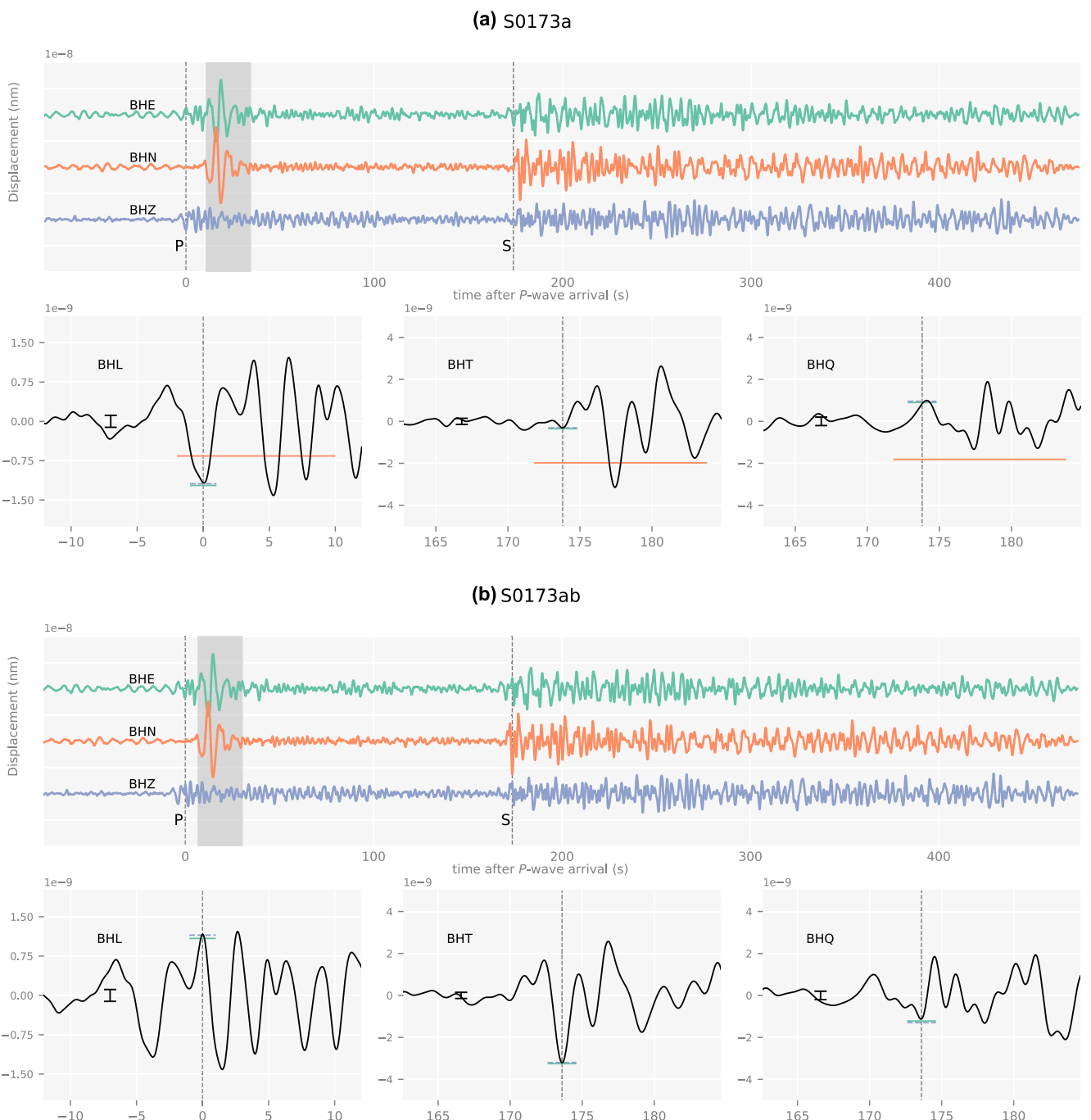


Figure 4. The long waveforms shown on the top of the figure are the E , N , and Z components. The L component shown on the bottom are zoomed-in to the P -wave arrival window while the T and Q components show the S -wave arrival window. The vertical black dashed line represents the first arrival times used for our analysis and the horizontal blue dashed lines are our measured amplitudes. The results of the modeled amplitudes for our best fitting fault mechanism solution is presented with the horizontal green line. Additionally, the red horizontal line represents the waveform amplitudes calculated from the mechanism published in Brinkman et al. (2021). The black error bar shown represents our estimated noise level and therefore the error estimation used in our analysis. All modeled amplitudes were computed using the New Gudkova model at a depth of 35 km. A glitch was also found and was marked by the gray box.

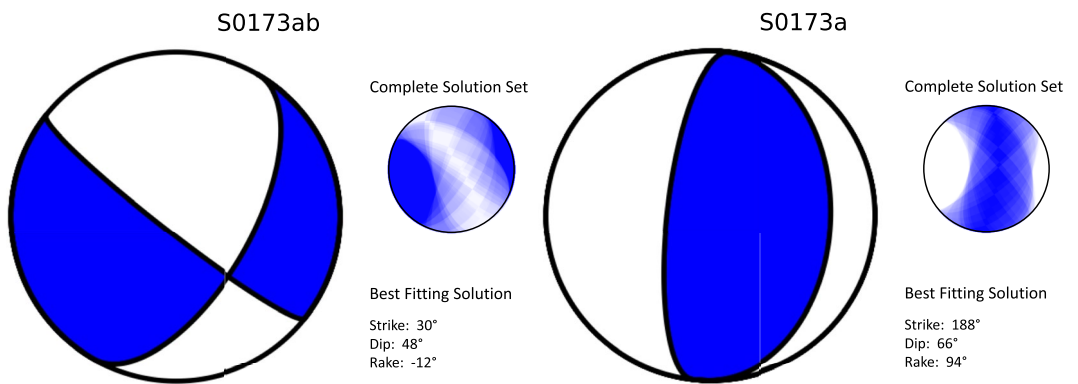


Figure 5. Presented is the best fitting solution for events S0173a and S0173ab at 35 km using the New Gudkova interior structure model. The complete set of solutions is also presented to show the error estimate of the fault plane determination.

the synthetic amplitudes produced for InSight's mechanism more closely resemble the motion over an entire inversion time window as the increased *SH* and *SV* energy predicted is inconsistent with our amplitude measurements of the first-arriving direct body waves. By taking this into consideration, we considered our source mechanisms for S0173a and S0173ab as the minor and major double couple components of a composite source mechanism, computed by summing the associated moment tensors for the major and minor double couple mechanisms (Figure 10). The second mechanism is weighted more heavily in this sum (weight = 0.6) than the first (weight = 0.4) on account of the overall larger amplitudes of the recorded body waves in the later portion of the time window.

Our composite source mechanism successfully recreates the InSight mission team's vertical dip-slip mechanism. The two mechanisms we presented were estimated from the amplitudes of two sets of seemingly direct body waves

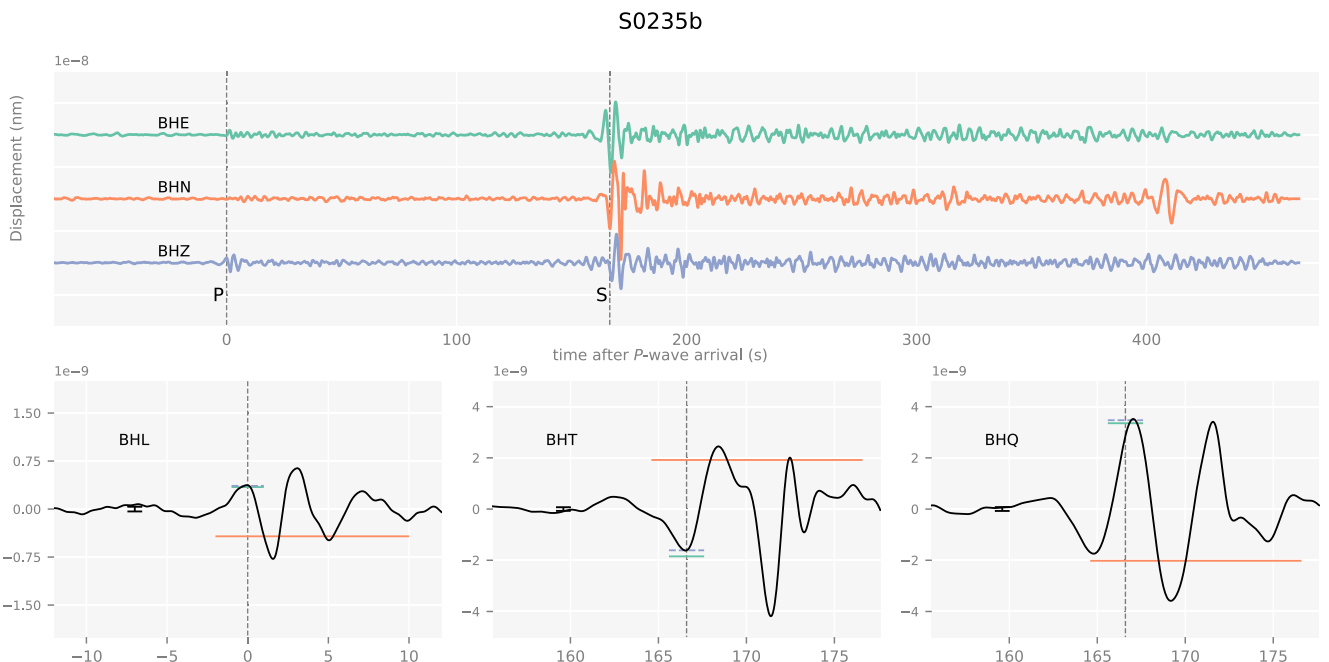


Figure 6. The long waveforms shown on the top of the figure are the *E*, *N*, and *Z* components. The *L* component shown on the bottom are zoomed-in to the *P*-wave arrival window while the *T* and *Q* components show the *S*-wave arrival window. The vertical black dashed line represents the first arrival times used for our analysis and the horizontal blue lines are our measured amplitudes. The results of the modeled amplitudes for our best fitting fault mechanism solution is presented with the horizontal green line. Additionally, the red horizontal line represents the waveform amplitudes calculated from the mechanism published in Brinkman et al. (2021). All modeled amplitudes were computed using the New Gudkova model at a depth of 35 km. The black error bar shown represents our estimated noise level and therefore the error estimation used in our analysis.



Figure 7. Presented is the best fitting solution for event S0235b at 35 km using the New Gudkova interior structure model. The complete set of solutions is also presented to show the error estimate of the fault plane determination.

that arrived 4 s apart, with identical $S-P$ differential travel times. It is possible that these two mechanisms mark the sudden beginning and sudden end of a 4 s long event, or are brittle side effects of a more prolonged, non-seismic event such as magmatic activity.

Rubin (1992) showed how propagating magmatic dikes can induce volcano-tectonic faulting in its surroundings by changing stresses in different ways in different areas surrounding the dike. Roman and Cashman (2006) add that volcano-tectonic quakes with different characteristics can also be induced by dike inflation. These stress fields move and change with the dike as it propagates and stalls, allowing for a range of faulting mechanisms in the vicinity of underground magmatic activity. Events S0173a and S0173ab could be due to such a magma intrusion, as the start, propagation, and stalling of a dike intrusion creates changes in the stress field with potential to generate earthquakes (Roman & Cashman, 2006; Rubin, 1992). Additionally, migrating magma or buoyancy loading can create opposite stresses on different sides of the intrusion (Farrell et al., 2009). On Earth, hydrothermal fluids escaping from rising magma within the crust have been suggested to find their way to existing fault planes causing a sudden onset and sudden

halt of earthquake swarms, in which different earthquakes in the swarm can have different faulting mechanisms (Roman & Cashman, 2006; Rubin, 1995; Shelly et al., 2013). We do not know whether Martian magma releases fluids deep within the Martian crust, but they may not be needed for a rising dike or plume(s) of magma to cause different types of sudden slip within the brittle lithosphere on different sides of their whereabouts.

It is unlikely that S0173ab is dynamically triggered by seismic waves of S0173a because S0173a's seismic waves seem too weak to generate sufficient stresses and do not travel fast enough if the mean epicenters are correct. However, the two epicenters for S0173a and S0173ab are within each other's error ellipses and therefore we cannot rule out that they could be co-located and represent opposite slip directions on the same fault. Something

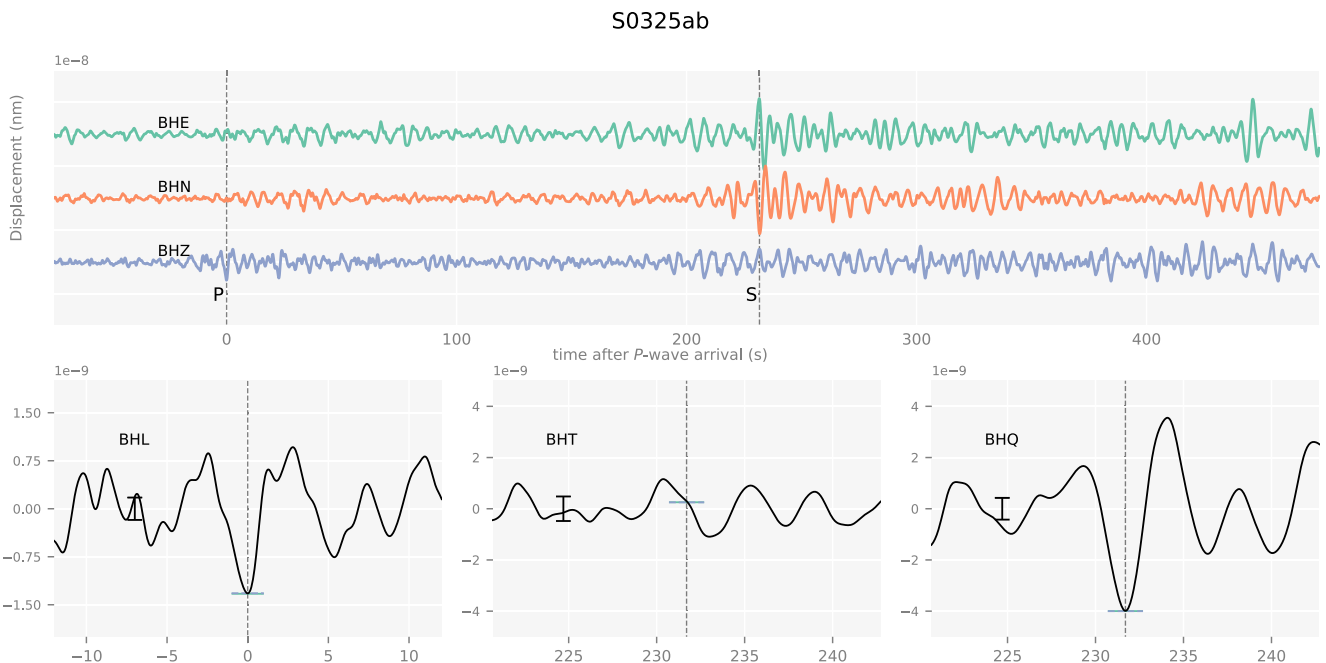


Figure 8. The long waveforms shown on the top of the figure are the E , N and Z components. The L component shown on the bottom are zoomed-in to the P -wave arrival window while the T and Q components show the S -wave arrival window. The vertical black dashed line represents the first arrival times used for our analysis and the horizontal blue lines are our measured amplitudes. The results of the modeled amplitudes for our best fitting fault mechanism solution is presented with the horizontal green line. The black error bar shown represents our estimated noise level and therefore the error estimation used in our analysis. All modeled amplitudes were computed using the New Gudkova model at a depth of 35 km.

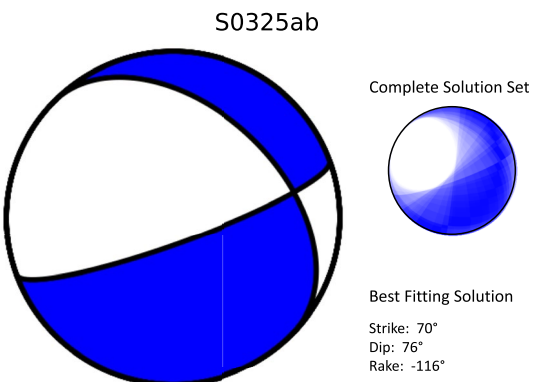


Figure 9. Presented is the best fitting solution for event S0325ab at 35 km using the New Gudkova interior structure model. The complete set of solutions is also presented to show the error estimate of the fault plane determination.

like this can be caused by a volume of magma that propagates as a dike intrusion, then cools, stalls, or partially deflates some seconds later, activating slip on fractures or faults in surrounding rock. A recent analysis by Sun and Tkalcic (2022) found many marsquakes in the area of Cerberus Fossae, many of which have smaller signal to noise ratios than S0173a but contain similar waveforms. Based on this repetitive nature of the seismicity, Sun and Tkalcic (2022) concluded that a magmatic origin was the most likely explanation.

The best-fitting faulting mechanism for S0235b has one relatively horizontal and one relatively vertical potential fault plane, just like the faulting mechanisms estimated by the InSight team for this event. The strikes of the vertical planes in the various estimates are relatively aligned with each other as well as with the strike of Cerberus Fossae. However, the *P* and *T* axes of our mechanism, with a slight reverse faulting component, are flipped with respect to those of the InSight team's mechanism, which shows normal faulting (Brinkman et al., 2021). We postulate that this flip in polarity of predicted body wave amplitudes between our's and the InSight team's mechanism is a

result of emphasizing different parts of the 10+ seconds-long *P* and *S* wave trains, which begin at very low amplitudes and grow increasingly above the noise level with time (Figure 6). We cannot exclude that this body wave train represents arrivals from a doublet event, perhaps with opposing faulting mechanisms, but for the moment we prefer the simpler solution of picking the *P* and *S* amplitudes at the earliest time they are significantly above the noise. The InSight team's waveform fitting approach emphasizes later, higher amplitude parts of the body wave trains, resulting in a similar faulting mechanism as ours, but with opposite polarity. As shown in Appendix A, using a different Mars model weights different possible solutions somewhat differently, but does not include normal faulting.

Our investigation of the third event, S0325ab, generated questions and uncertainties as its signals are weaker and did not seem to originate from the Cerberus Fossae region. The body wave arrival times for S0325ab are listed in Table 2. The epicenter for event S0325ab falls near the boundary between the Martian highlands in the south and the lowlands in the north. Based on orbital images provided by Knapmeyer et al. (2006), there are a number of tensional and compressional faults in the general region. The lack of depth resolution in our methods lead to uncertainties in the true depth of the event and, therefore, the inferred fault planes might be sufficiently deep to not require a resemblance to surface faults. Recently Zenhäusern et al. (2022) estimated epicenters for events S0105a, S0784a, S0918a, in this same region.

As discussed earlier, S0325ab was initially identified as a secondary arrival of a doublet event. Analysis showed that the seismic waves from the primary event, S0325a, had even lower signal to noise ratios than those from

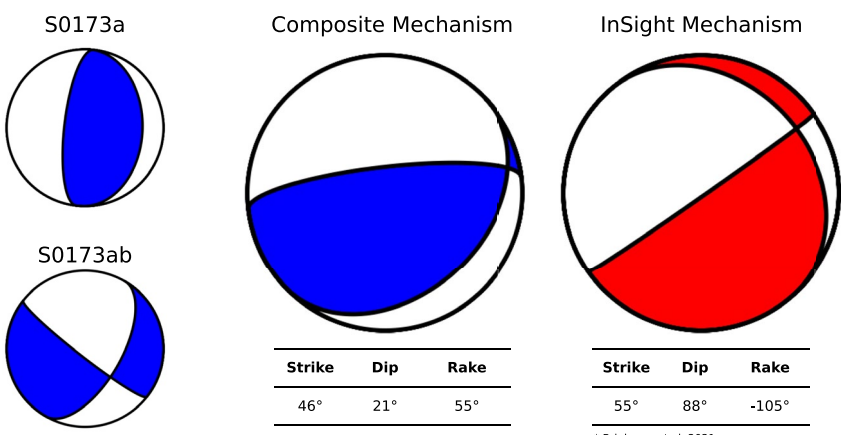


Figure 10. The moment tensors for S0173a and S0173ab shown on the left were combined with weights of 0.4 and 0.6 respectively to produce the composite mechanism.

S0325ab and proved insufficient to either confidently locate its epicenter or constrain its faulting mechanism. Figure 2 shows two possible locations for the epicenter of S0325a and Appendix B shows the associated faulting mechanisms for each location. The possible faulting mechanism for the potential epicenter north-east of the lander has a strong strike-slip component. Conversely, the possible faulting mechanism for the potential epicenter south-east of the lander represents normal faulting with a roughly east-west oriented T axis. Both mechanisms differ from the estimated faulting mechanism for S0325ab, the clearer and stronger event (Figure 9). We have a slight preference for the south-east location for S0325a, because it would allow the S0325a and S0325ab doublet to have a similar volcano-tectonic origin as discussed above for S0173a and S0173ab. However, we decided not to further consider this event on account of the low signal-to-noise ratio of the body wave arrivals.

The results presented here are uncertain to reported extents and may be limited due to the following assumptions:

1. The arrival times for the P - and S -waves reported by the MQS are correct,
2. All arrivals used for amplitude measurements were direct body waves, rather than surface-reflected waves or waves reflected or converted at a layer boundary,
3. The faulting mechanisms associated with the marsquakes are pure double-couple mechanism (pure shear dislocations),
4. The seismic velocity model used has a minimal effect on the calculation of synthetic waveform amplitudes,
5. Hypocentral depth used during the investigation has minimal effect on the resulting best fitting mechanism produced by our methods.

Assumptions 1 and 2 have been verified to the best of our current abilities, as discussed above. Assumption 3 was deemed reasonable as Brinkman et al. (2021) suggests that the contributions from non-double-couple components in the mechanisms are small. Assumptions 4 and 5 have been verified within existing uncertainties and are further discussed in Appendix A.

5. Conclusions

The InSight mission produced a rich, fascinating collection of seismic waveforms recorded on Mars. Among the first set of seismic events reported by the MQS were three relatively low-frequency events with measurable P and S displacement amplitudes, particle motion, and differential arrival times. These events had small magnitudes and were recorded with relatively low signal-to-noise ratios in an unfamiliar noise environment. Although we have estimated errors, some errors are not as easily quantifiable, for example, as related to phase identification by us or the InSight Marsquake Service (2021). To counteract these uncertainties, we provided all data processing details in this paper, for readers to evaluate.

We estimated epicenters for these events by measuring the arrival time difference between P and S waves in three-component data from the Very Broad Band (VBB) seismometer installed as part of the mission and by estimating back azimuths from minimizing P energy on the T component and validating the results with visualized particle motion directions. Our estimated epicenters for S0173a and S0235b are near Cerberus Fossae, east of the lander, and agreed well with those determined by the InSight team (Brinkman et al., 2021). We additionally located event S0325ab to the south-east of the lander, near the border between the northern lowlands and southern highlands of Mars.

These representative low-frequency marsquakes are low in magnitude and likely occur relatively deep in a thick, rigid crust or the upper mantle, so they are unable to generate notable surface waves, which are a common tool for estimating faulting mechanisms on Earth. Instead, we estimated shear dislocation faulting mechanisms for these events by fitting the relative P and S wave displacement amplitudes.

In order to compare observed and computed relative P and S amplitudes in a robust manner that allows for vanishing amplitudes and the conservation of polarity, we defined and present a new, geometric definition of fit. Along with this robust misfit definition, we also provide a misfit tolerance that depends on the observational noise levels, estimated from the displacement waveforms' standard deviation before the arrival of body waves. The mechanisms for the marsquakes in the Cerberus Fossae region range from near-vertical dip slip along a fault plane that strikes roughly parallel to the fossae, to compressional and transtensional faulting. The faulting mechanism for the event south-east from the lander is also transtensional though with a different T axis azimuth than the transtensional event near Cerberus Fossae.

It is possible that S0173a was a doublet composed of two events, 4 s apart, with epicenters within each other's error ellipses. The best-fitting faulting mechanism for the first event, S0173a, is a reverse faulting mechanism with an east-west oriented P axis. The best-fitting faulting mechanism for the second event, S0173ab, has a P axis that is one quadrant rotated from that for S0173a, and a near-horizontal T axis, that is, representing oblique strike-slip or transtensional faulting. A weighted linear combination of these two successive mechanisms produces a composite mechanism that resembles the source mechanism estimated by the InSight Team from waveform modeling of the entire wave train in and beyond the time window analyzed (Brinkman et al., 2021).

The best-fitting faulting mechanism for event S0235b is a near vertical dip-slip mechanism. The alignment between the vertical fault plane and the Cerberus Fossae suggests that the fossae may indeed be tectonically active features. However, this mechanism is different from the normal faulting solution presented by Brinkman et al. (2021). We consider this disagreement to likely be a result of the differences between our choice in time window used to measure the direct waves' amplitudes and for waveform fitting of the InSight team. We cannot rule out that S0235b also represents a doublet of two events, which would have occurred in rapid succession.

Lastly, for S0325ab, the best-fitting faulting mechanism was an oblique normal faulting mechanism with a roughly north-east oriented and slightly tilted T and P axes. It is possible that event S0325ab was a second event in a doublet, but the seismic waves generated by the preceding event had an insufficient signal to noise ratio to constrain either its epicenter or its faulting mechanism (see Appendix B).

The diversity of these epicenters and fault plane solutions suggest that a range of intraplate tectonic or volcanic processes might be operational in the Martian lithosphere. We argue in the Discussion section above that a likely explanation for these marsquakes is that they are the result of changing stresses concomitant with migrating magma in the lower crust, including propagating dikes.

Our work independently confirms some of the analyses of the InSight team (Brinkman et al., 2021; Giardini et al., 2020; Zenhäusern et al., 2022), and provides additional detail and perspective. Overall, our multifaceted analyses of observed body waves from three low-frequency marsquakes produced plausible results, allowing this investigation to work as a proof of concept for applying this method to additional data collected by InSight as well as data collected on future missions to other potential planetary bodies or low-magnitude earthquakes in sparsely instrumented regions.

Marsquakes in the current data set have come from a variety of different locations, including Cerberus Fossae, and the P- and S-wave amplitudes can be explained by a range of faulting mechanisms, including normal, reverse, oblique strike-slip, and vertical dip-slip faulting. Our concluding hypothesis is that these marsquakes are the result of volcano-tectonic stresses related to magmatic processes active in Mars' lower crust.

Appendix A: The Effect of Depth and Model Choice on Event Solution Output

In this appendix we present the results of our investigation of the choice of hypocentral depth and interior structure model on the solution set output of our methods. Overall, the preferred mechanisms presented in this paper appeared in the top 1% of solutions however it was not always the best fitting solution for every model and at every depth tested.

The faulting mechanism presented for S0235b using the New Gudkova model at a depth of 35 km is a near vertical dip-slip mechanism is also preferred by the same model at a deeper 55 km depth (Figure A1a). At shallower depths for this model a purely compressional fault with different fault plane strikes is preferred. This is the preferred solution among the other models across all depths, except for the A1c model, which also shows a vertical dip-slip mechanism, albeit with a slightly different fault strike (Figure A1).

S0173a and S0173ab showed similar behavior across depths and models tested. The complete solution set of all possible mechanisms remains stable but which of the well-fitting mechanisms becomes the best-fit one differs slightly with depth and model and less so than for S0235b. Similar to what is shown in Figure 5, S0173a is dominated by reverse faults with an almost N-S striking fault plane and S0173ab is modeled by predominately normal faulting with a strike-slip component. This is true across all depths and models tested.

The orientations for the complete set of solutions for S0325ab were less stable across depth and models tested, however a tensional mechanism was preferred throughout.

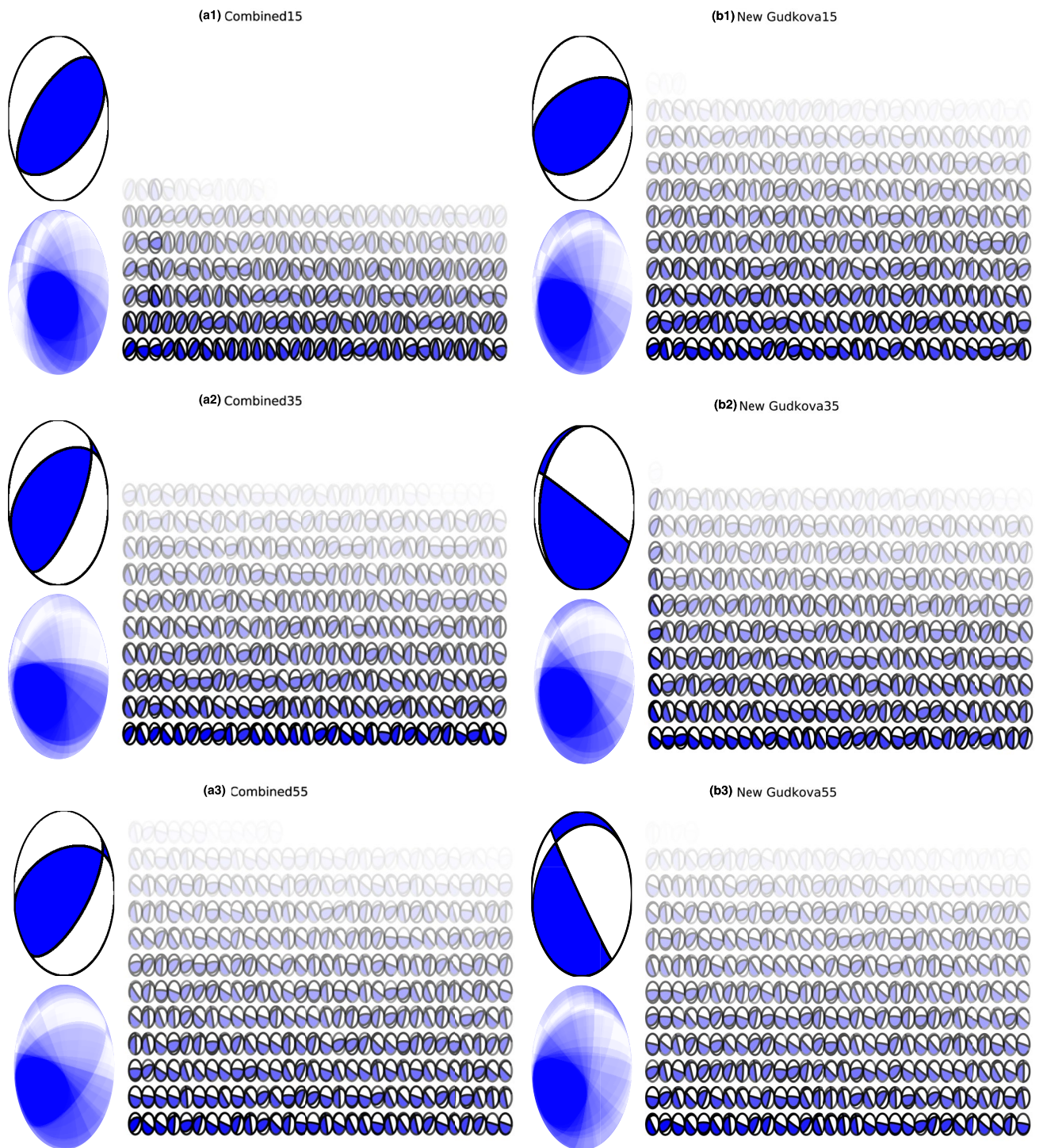


Figure A1. The complete set of solutions across multiple depths and models for event S0235b. The best fitting mechanisms correspond to the darker beachballs while worst fitting mechanisms that are still permissible correspond to the transparent beachballs. (a) The complete set of results for S0235b using the depths of 15, 35, and 55 km and the New Gudkova model. (b) The complete set of results for S0235b using the depths of 15, 35, and 55 km and the Combined model. (c) The complete set of results for S0235b using the depths of 15, 35, and 55 km and the TAYAK model.

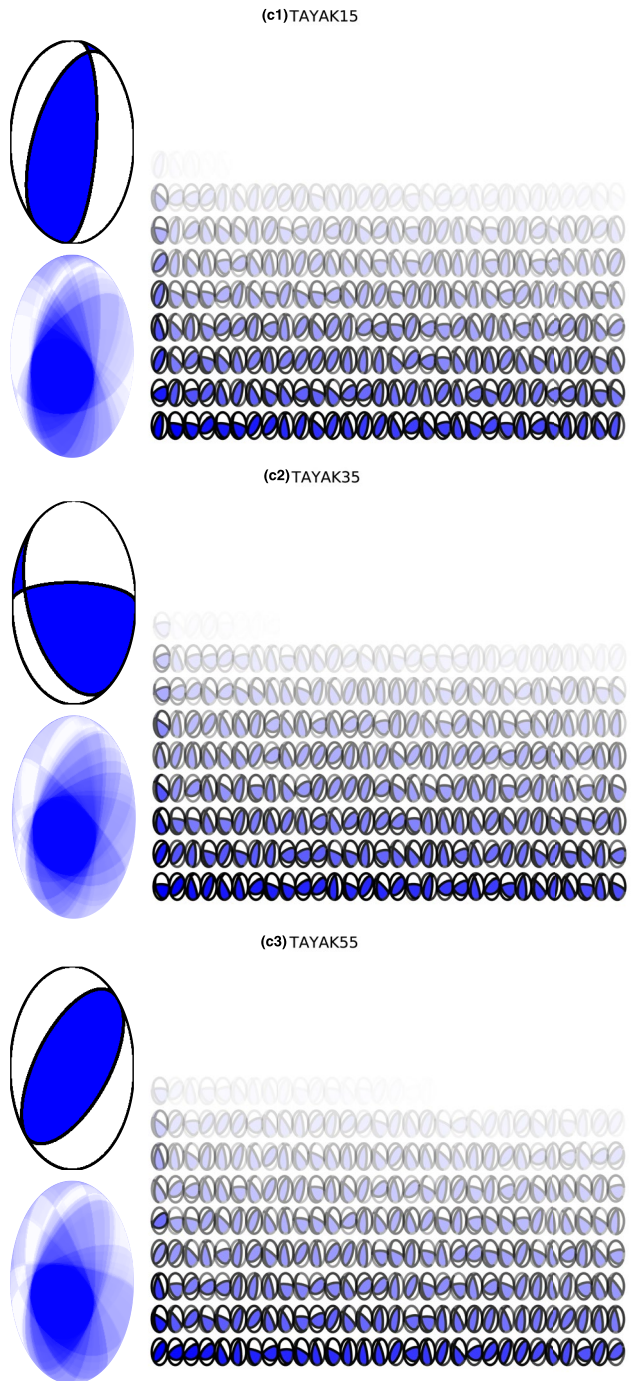


Figure A1. (Continued)

Appendix B: Further Investigation of S0325a

Presented in this appendix are the results of our analysis of the event S0325a. Figure B1 shows the measured and predicted body wave amplitudes for the two possible locations for S0325a presented in Figure 2. Figure B2 shows the body waves' low-signal-to-noise ratios and ambiguous polarization, which allow for two possible locations. Lastly, for each possible epicenter, Figure B3 shows the complete solution set of acceptable faulting mechanisms.

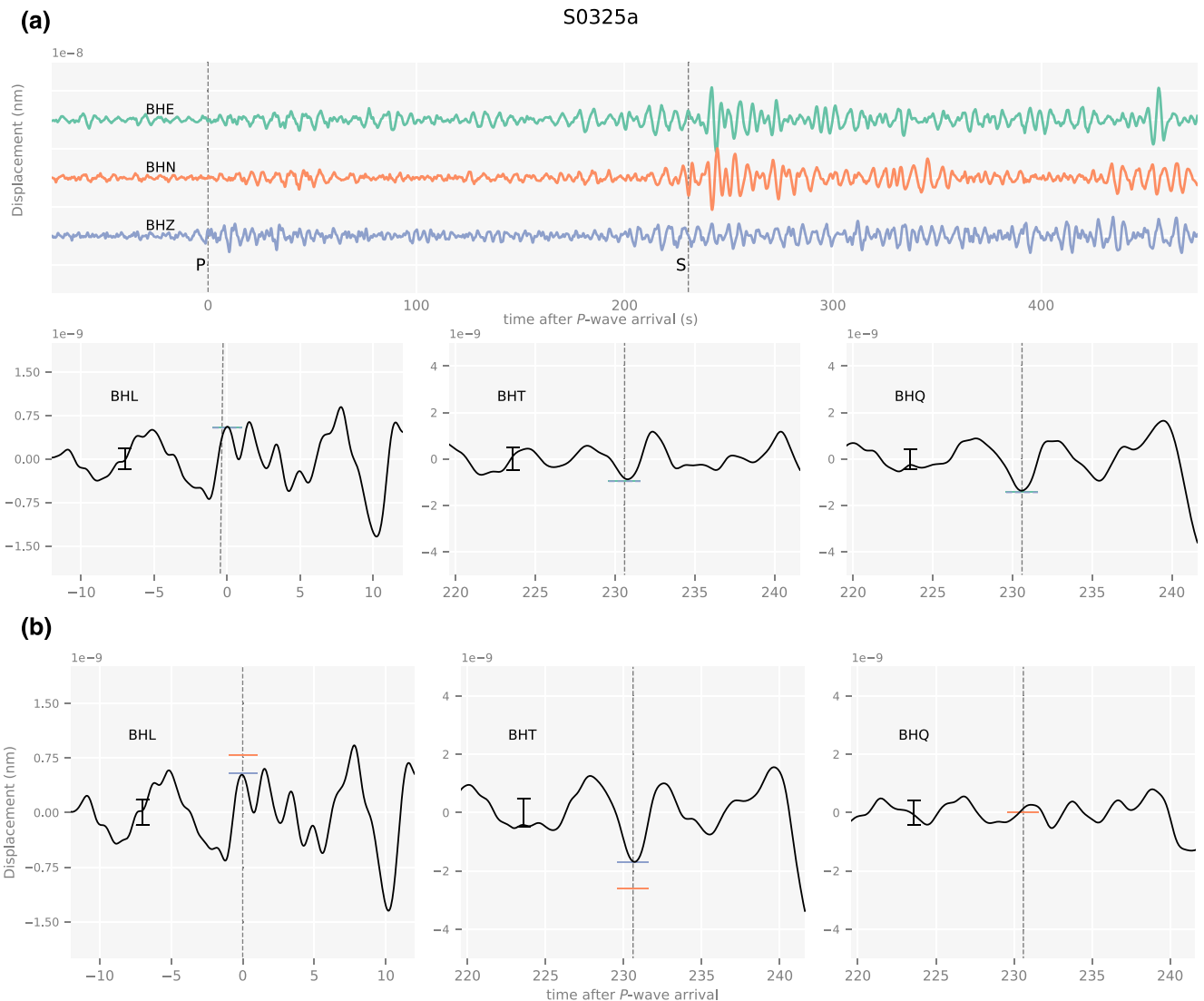


Figure B1. The long waveforms shown on the top of the figure are the E , N , and Z components. The L component shown on the bottom are zoomed-in to the P -wave arrival window while the T and Q components show the S -wave arrival window. The vertical black dashed line represents the first arrival times used for our analysis and the horizontal blue lines are our measured amplitudes. The black error bar shown represents our estimated noise level and therefore the error estimation used in our analysis. All modeled amplitudes were computed using the New Gudkova model at a depth of 35 km. (a) The results of the modeled amplitudes for the best fitting fault mechanism solution given our calculated back azimuth of 123° is presented with the horizontal green line. (b) The results of the modeled amplitudes for the best fitting fault mechanism solution given the back azimuth of 57° is presented with the horizontal orange line.

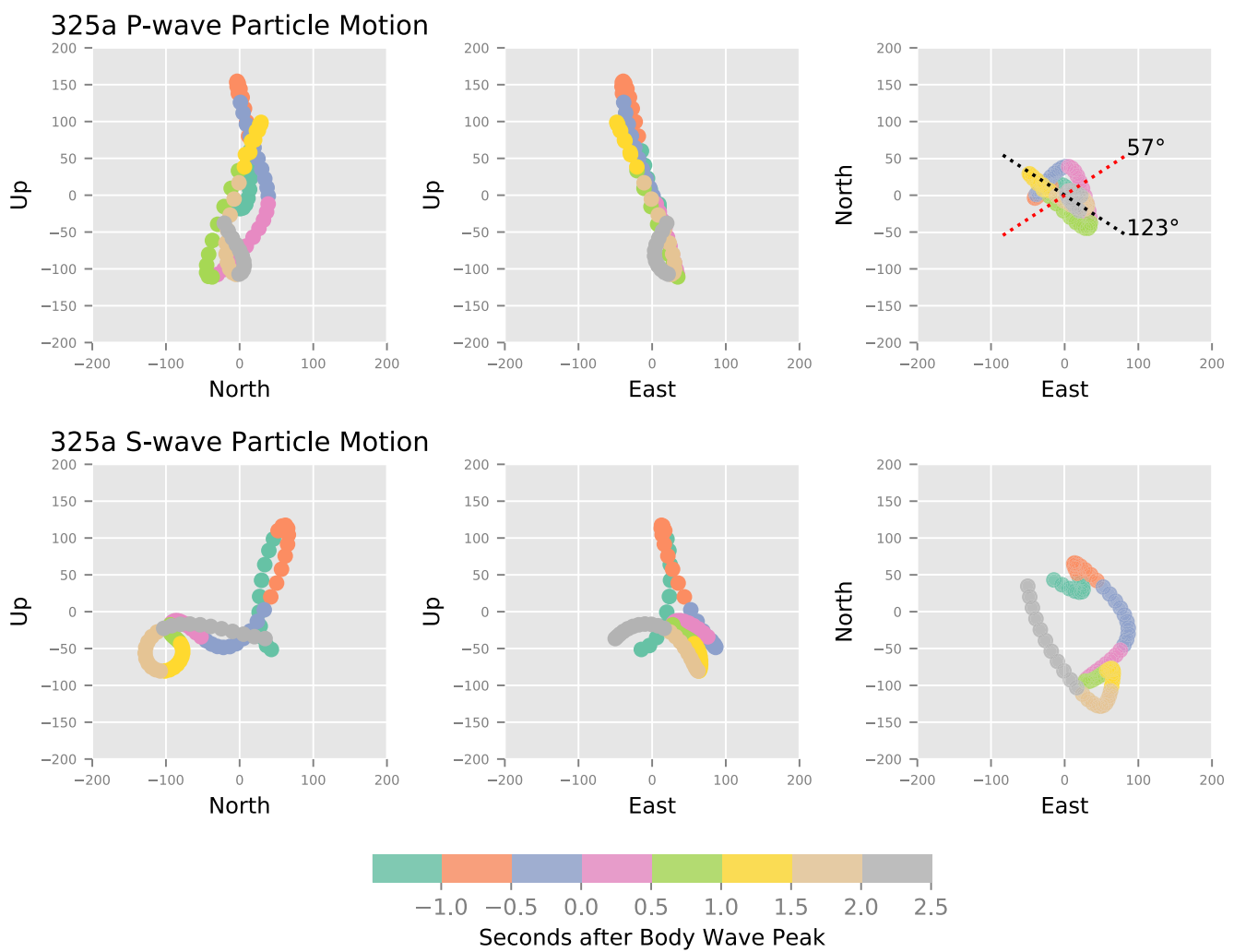


Figure B2. The three particle motion cross sections of *P*-wave and *S*-wave arrival times for each event are shown. Each color represents 0.5 s of data. A black dashed line is shown to highlight the back azimuth determined in our analysis, 123° and a red dashed line shows the back azimuth of 57° presented in Zenhäusern et al. (2022).

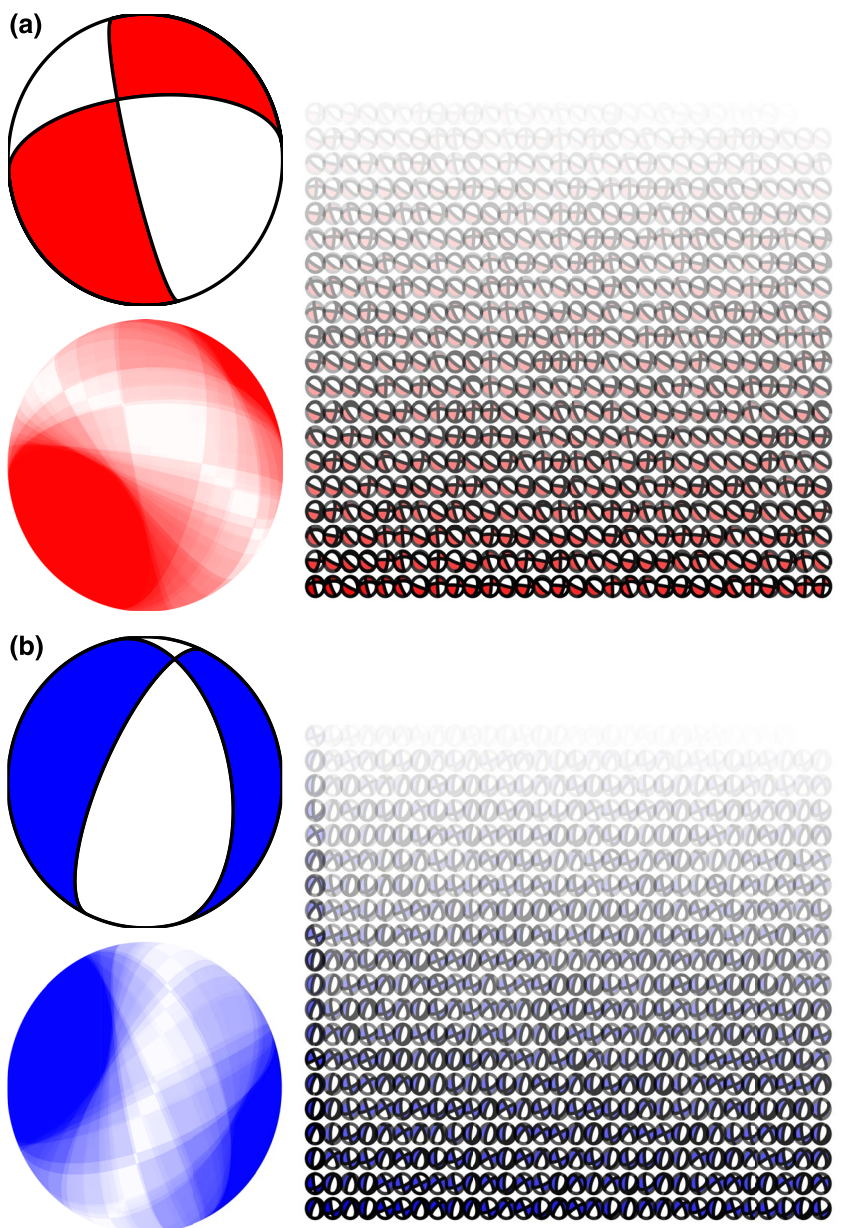


Figure B3. Using a depth of 35 km and the New Gudkova model, the complete set of possible solutions were computed for S0325a. The best fitting mechanisms correspond to the darker beachballs while the worst fitting mechanisms, that are still permissible, correspond to the transparent beachballs. (a) The complete set of solutions given a back azimuth of 57°. (b) The complete set of solutions given a back azimuth of 123°.

Appendix C: Complete Sets of Beachball Solutions

Presented in Figures C1, C2, and C3 are the complete collections of acceptable double-couple solutions for each of the events discussed in the main body of this paper. These fault plane solutions are deemed acceptable as their misfit values calculated using our definition fall below the tolerance value set by the error estimated from the noise level of each seismogram.

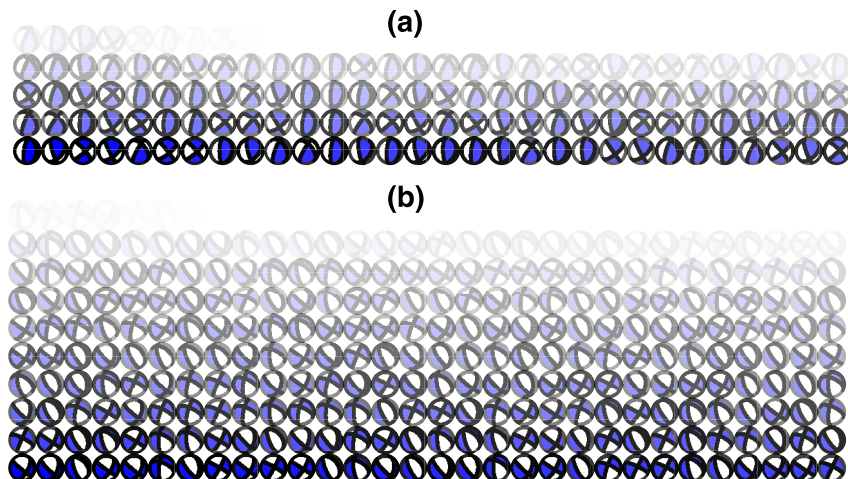


Figure C1. The complete set of solutions for S0173a and S0173ab at our chosen depth of 35 km for the New Gudkova model. The best fitting mechanisms correspond to the darker beachballs while worst fitting mechanisms that are still permissible correspond to the transparent beachballs. (a) The complete set of results for S0173a using a cutoff value of 0.024 radians. (b) The complete set of results for S0173ab using a cutoff value of 0.034 radians. The ideal depth of 35 km was used for both figures along with the New Gudkova model.

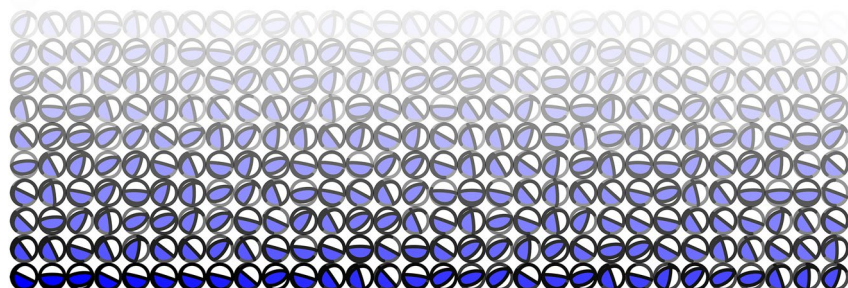


Figure C2. The complete set of results for S0235b using the New Gudkova model at a depth of 35 km and a cutoff value of 0.025 radians. The best fitting mechanisms correspond to the darker beachballs while worst fitting mechanisms that are still permissible correspond to the transparent beachballs.

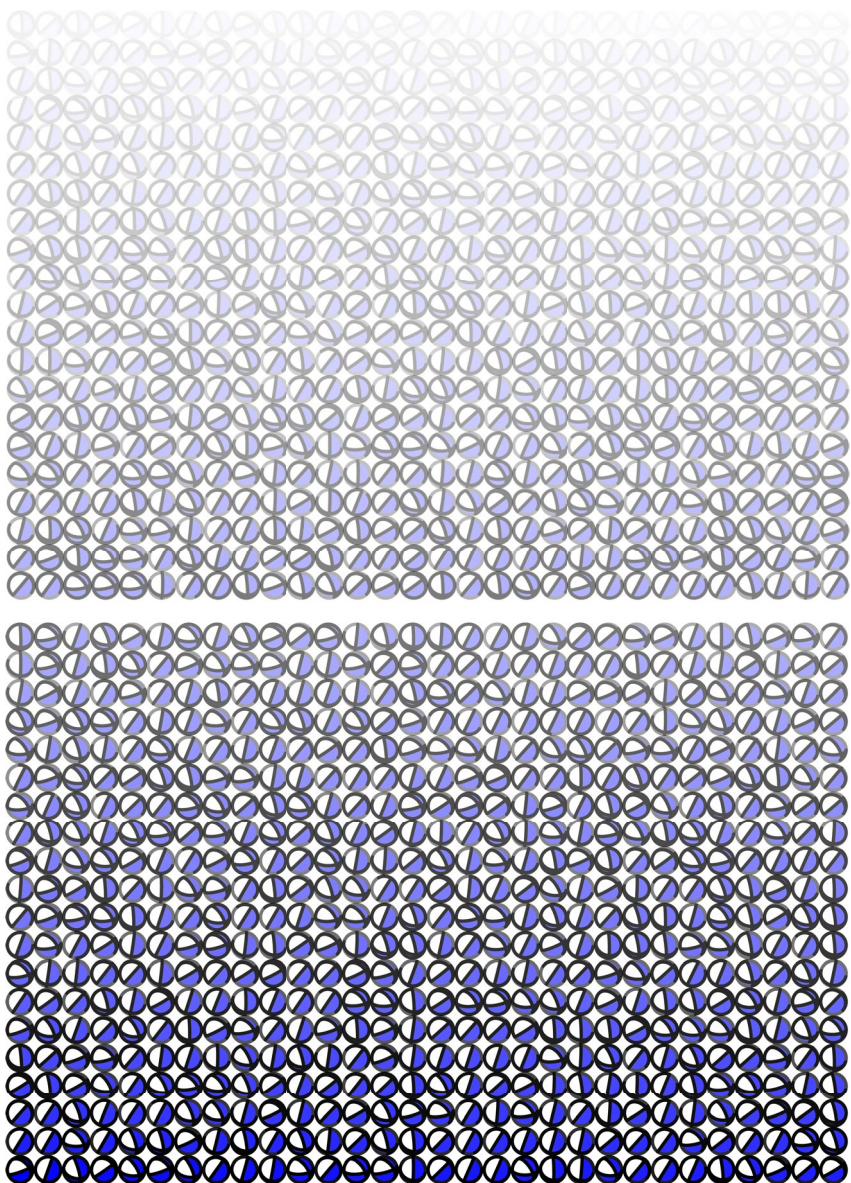


Figure C3. The complete set of results for S0325ab using the New Gudkova model at a depth of 35 km and a cutoff value of 0.054 radians. The best fitting mechanisms correspond to the darker beachballs while worst fitting mechanisms that are still permissible correspond to the transparent beachballs.

Appendix D: Earthquake Test

The methods used for determining the faulting mechanism solutions were validated using a randomly selected earthquake that occurred on 10 October 2021, SSE of Naalehu, Hawaii. The reference faulting mechanism for this earthquake is shown in Figure D4. Using the source parameters published on the USGS website for the Earthquake Hazard Program (USGS, 2021), we calculated the first motion amplitudes of the waveforms upon their arrival at two different stations of the Global Seismograph Network (Albuquerque Seismological Laboratory (ASL)/USGS, 1988).

We measured P , SV , and SH displacement amplitudes of 1.04, -1.55, and $-2.74 \pm 0.10 \mu\text{m}$ in data recorded in Albuquerque, New Mexico, at station ANMO as shown in Figure D1. Using station COR in Corvallis, Oregon, we measured P , SV , and SH displacement amplitudes of 1.54, -2.19, and $-2.34 \pm 0.10 \mu\text{m}$ (Figure D2). All faulting mechanisms that produce well fitting relative amplitudes to these observations are shown in Figures D3 and D5.

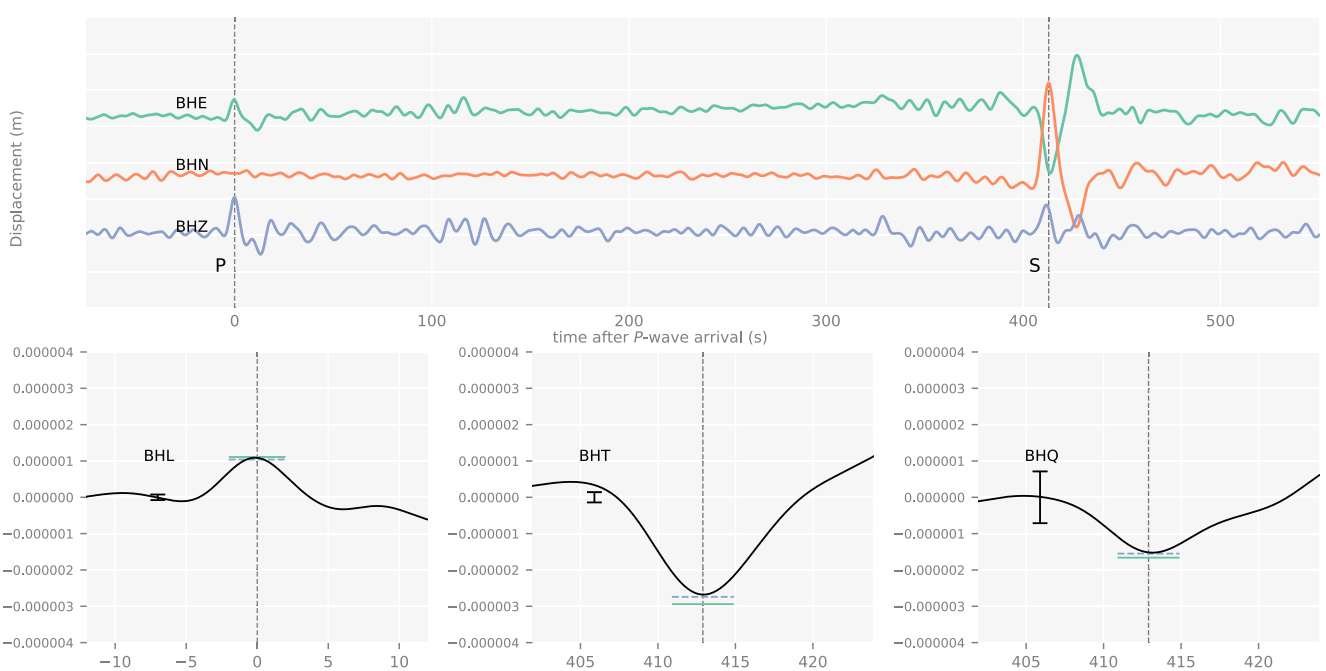


Figure D1. ANMO Station: The black dashed line represents the arrivals used for our analysis. The results of the modeled amplitudes for our best fitting fault mechanism solution based on the amplitudes gathered from station ANMO is presented with the horizontal orange line.

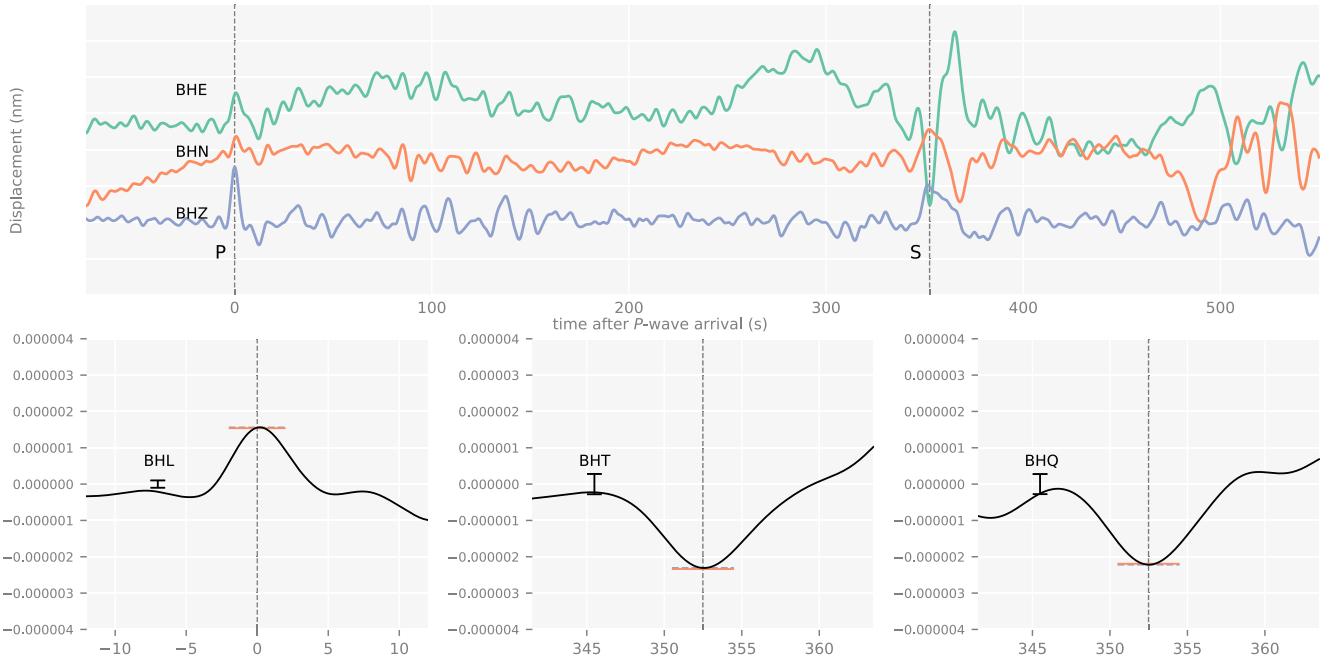


Figure D2. COR Station: The black dashed line represents the arrivals used for our analysis. The results of the modeled amplitudes for our best fitting fault mechanism solution based on the amplitudes gathered from station COR is presented with the horizontal green line.

Figure D4 shows that the best fitting mechanism has similar fault planes and principal axes as the official USGS mechanism, as is true for many of the solutions producing acceptable relative amplitude fits to the observations.

However, solutions that are similar to the official solution are not the only solutions that fit the observation. Other groups of mechanism can produce acceptable relative amplitude fits. What these mechanisms have in common

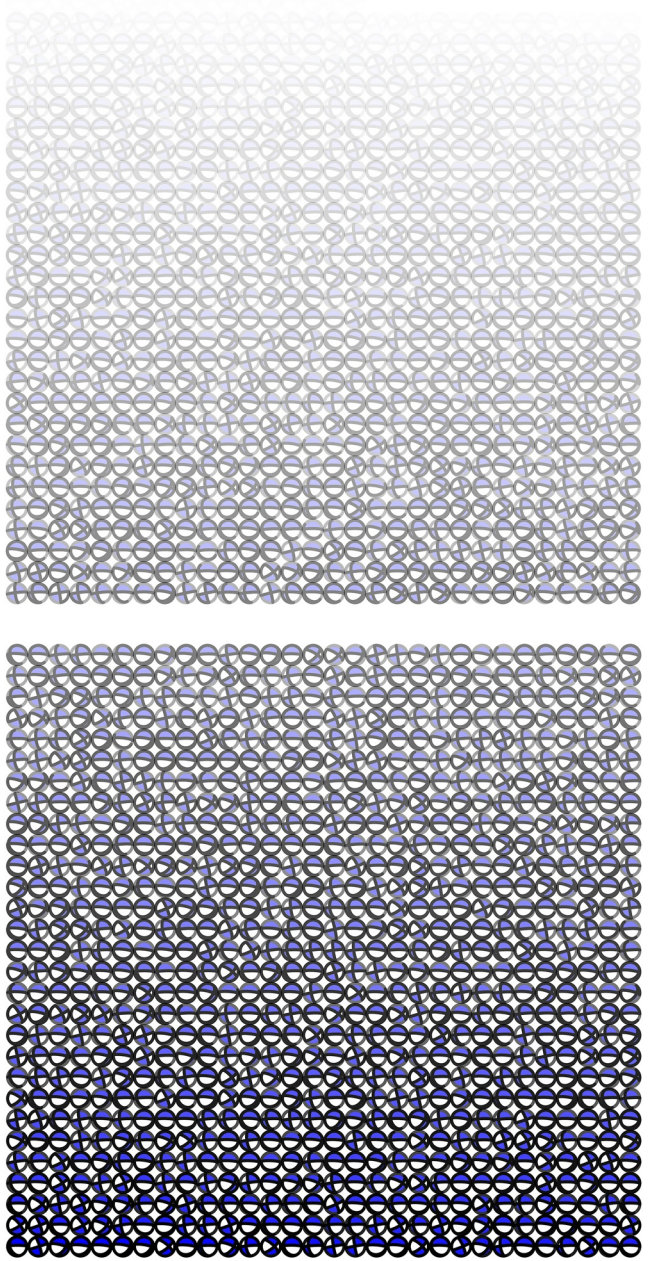


Figure D3. The complete set of solutions produced by the amplitudes recorded at ANMO for the 10 October 2021 earthquake, SSE of Naalehu, Hawaii. The best fitting mechanisms correspond to the darker beachballs while worst fitting mechanisms that are still permissible correspond to the transparent beachballs.

is a T axis northwards from the take-off azimuth and a relatively vertical W-E striking fault plane. This group of mechanisms include vertical dip-slip mechanisms as well as strike-slip mechanisms, illustrating that body waves measured at one station can constrain faulting mechanisms, but not tightly. For this reason, and throughout this paper, we show all faulting mechanisms with acceptable fits, rather than only the best fitting ones.

Repeating this analysis for station COR reveals similar faulting mechanisms (Figure D5), where the best fitting mechanism represents oblique normal faulting or a tilted strike-slip mechanisms, while the second best fitting mechanism based off our misfit determination has fault planes and principal axes similar to the official one. However, we do not reproduce or attempt to reproduce the CLVD component of the mechanism published by the USGS.

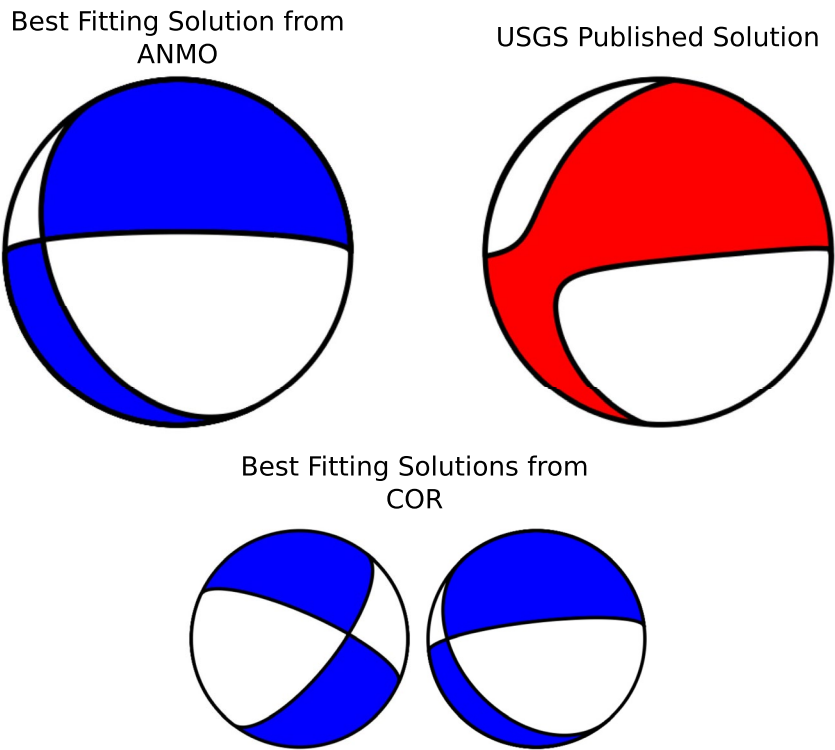


Figure D4. The best fitting solutions from station ANMO and COR as compared to the published solution by USGS (2021). The best fitting mechanisms correspond to the darker beachballs while worst fitting mechanisms that are still permissible correspond to the transparent beachballs.

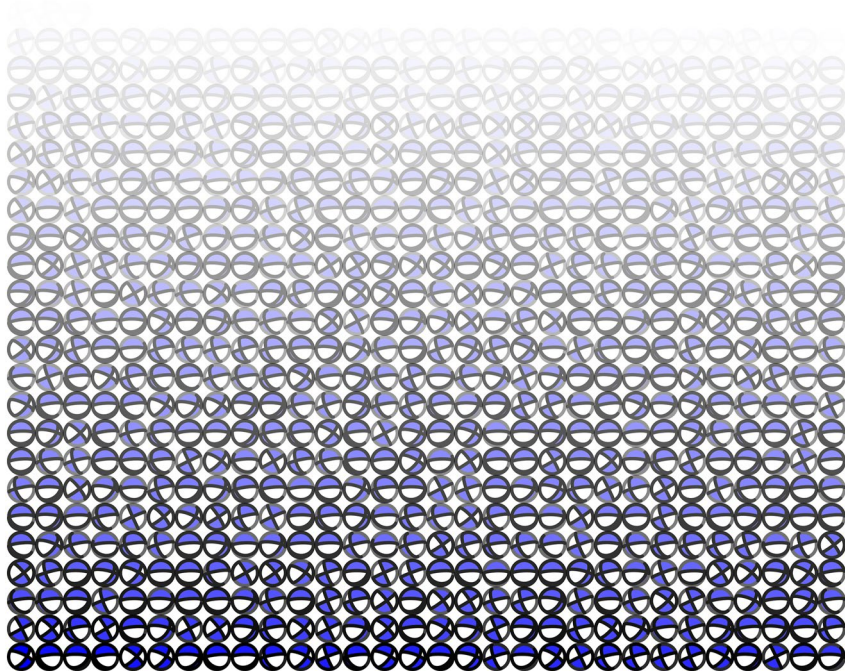


Figure D5. The complete set of solutions produced by the amplitudes recorded at COR for the 10 October 2021 earthquake, SSE of Naalehu, Hawaii.

Data Availability Statement

Data from the ESA/NASA InSight mission are publicly available through multiple portals including Data Services offered by IRIS (InSight Marsquake Service, 2020, 2022). We did not generate additional data. Visualizations were created with PyGMT (Wessel et al., 2019) and Matplotlib (Hunter, 2007), data were processed with NumPy (Harris et al., 2020), Pandas (The Pandas Development Team, 2021) and ObsPy (Krischer et al., 2015). Parameters describing our results are provided in tables and figures throughout this paper. The source code for the seismogram plots and moment tensor solution sets to produce Figures 4–9 are made available in a public repository (Sita, 2022).

Acknowledgments

This work was supported by the National Science Foundation under Grant No. AST-1757792, a Research Experiences for Undergraduates (REU) grant awarded to CIERA at Northwestern University. We acknowledge Aaron Geller, the director of the REU program, for all of his help throughout the first summer of this project as well as Mark Panning and Philippe Lognonné for providing information about the SEIS seismometer. We are grateful to many for their helpful discussions and encouragement, including Monique Holt, Ajay Limaye, Ann Thomas, and Jiaqi Li. We are grateful to Jochen Braunmiller and Mark Panning for their critical, comprehensive, and constructive, but most of all InSightful reviews that led us to significantly improve this paper.

References

- Aki, K., & Richards, P. G. (1980). *Quantitative seismology, theory and methods* (Vol. 854). Freeman & Co.
- Albuquerque Seismological Laboratory (ASL)/USGS. (1988). Global Seismograph Network: IRIS/USGS. International Federation of Digital Seismograph Networks. Retrieved from <https://www.fdsn.org/networks/detail/IU%20doi:%2010.7914/SN/IU>
- Banerdt, W., Smrekar, S., Banfield, D., Giardini, D., Golombek, M., Johnson, C., et al. (2020). Initial results from the insight mission on Mars. *Nature Geoscience*, 13(3), 1–7. <https://doi.org/10.1038/s41561-020-0544-y>
- Bertka, C. M., & Fei, Y. (1998). Density profile of an SNC model Martian interior and the moment-of-inertia factor of Mars. *Earth and Planetary Science Letters*, 157(1–2), 79–88. [https://doi.org/10.1016/s0012-821x\(98\)00030-2](https://doi.org/10.1016/s0012-821x(98)00030-2)
- Braunmiller, J., Nabelek, J., & Ghods, A. (2020). Sensor orientation of Iranian broadband seismic stations from P-wave particle motion. *Seismological Research Letters*, 91(3), 1660–1671. <https://doi.org/10.1785/0220200019>
- Brinkman, N., Stähler, S. C., Giardini, D., Schmelzbach, C., Khan, A., Jacob, A., et al. (2021). First focal mechanisms of marsquakes. *Journal of Geophysical Research: Planets*, 126(4), e2020JE006546. <https://doi.org/10.1029/2020JE006546>
- Buland, R., & Chapman, C. (1983). The computation of seismic travel times. *Bulletin of the Seismological Society of America*, 73(5), 1271–1302.
- Carr, M. (1999). Mars Beatty JK, Petersen CC, Chaikin A. The new solar system (pp. 141–156).
- Clinton, J., Giardini, D., Böse, M., Ceylan, S., Driel, M., Euchner, F., et al. (2018). The marsquake service: Securing daily analysis of seis data and building the martian seismicity catalogue for insight. *Space Science Reviews*, 214(8), 133. <https://doi.org/10.1007/s11214-018-0567-5>
- Clinton, J., Giardini, D., Lognonné, P., Banerdt, B., Driel, M., Drilleau, M., et al. (2017). Preparing for insight: An invitation to participate in a blind test for martian seismicity. *Seismological Research Letters*, 88(5), 1290–1302. <https://doi.org/10.1785/0220170094>
- Crotwell, H. P., Owens, T. J., & Ritsema, J. (1999). The taup toolkit: Flexible seismic travel-time and ray-path utilities. *Seismological Research Letters*, 70(2), 154–160. <https://doi.org/10.1785/gsrl.70.2.154>
- Dannemann Dugick, F. K., van der Lee, S., Prieto, G. A., Dybing, S. N., Toney, L., & Cole, H. M. (2021). Roses: Remote online sessions for emerging seismologists. *Seismological Society of America*, 92(4), 2657–2667. <https://doi.org/10.1785/0220200421>
- Dreibus, G., & Wanke, H. (1985). Mars, a volatile-rich planet. *Meteoritics*, 20, 367–381.
- Ebel, J., & Bonjer, K.-P. (1990). Moment tensor inversion of small earthquakes in southwestern Germany for the fault plane solution. *Geophysical Journal International*, 101(1), 133–146. <https://doi.org/10.1111/j.1365-246x.1990.tb00763.x>
- Farrell, J., Husen, S., & Smith, R. B. (2009). Earthquake swarm and b-value characterization of the Yellowstone volcano-tectonic system. *Journal of Volcanology and Geothermal Research*, 188(1–3), 260–276. <https://doi.org/10.1016/j.jvolgeores.2009.08.008>
- Giardini, D., Lognonné, P., Banerdt, W. B., Pike, W. T., Christensen, U., Ceylan, S., et al. (2020). The seismicity of Mars. *Nature Geoscience*, 13(3), 205–212.
- Gutenberg, B., & Richter, C. (1941). *Seismicity of the Earth* (Vol. 34). Geological Society of America.
- Hardebeck, J. L., & Shearer, P. M. (2003). Using s/p amplitude ratios to constrain the focal mechanisms of small earthquakes. *Bulletin of the Seismological Society of America*, 93(6), 2434–2444. <https://doi.org/10.1785/0120020236>
- Harris, C. R., Millman, K. J., van der Walt, S. J., Gommers, R., Virtanen, P., Cournapeau, D., et al. (2020). Array programming with NumPy. *Nature*, 585(7825), 357–362. <https://doi.org/10.1038/s41586-020-2649-2>
- Hunter, J. D. (2007). Matplotlib: A 2D graphics environment. *Computing in Science & Engineering*, 9(3), 90–95. <https://doi.org/10.1109/MCSE.2007.55>
- InSight Marsquake Service. (2020). Mars seismic catalogue, insight mission; v2 2020-04-01 (version 2.0) [Dataset]. ISAESupaero,. <https://doi.org/10.12686/a7>
- InSight Marsquake Service. (2021). Mars seismic catalogue, insight mission; v8 2021-10-01 (version 8.0) [Dataset]. ETHZ, IPGP, JPL, ICL: University of Bristol. <https://doi.org/10.12686/a13>
- InSight Marsquake Service. (2022). Mars seismic catalogue, InSight mission; V9 2022-01-01 (version 9.0) [Dataset]. ETHZ, IPGP, JPL, ICL, University of Bristol. <https://doi.org/10.12686/a14>
- InSight Mars SEIS Data Service. (2019). Seis raw data, insight mission. IPGP, JPL, CNES, ETHZ, ICL, MPS, ISAE-Supaero, LPG, MFSC. https://doi.org/10.18715/SEIS.INSIGHT.XB_2016
- Kedar, S., Panning, M. P., Smrekar, S. E., Stähler, S. C., King, S. D., Golombek, M. P., et al. (2021). Analyzing low frequency seismic events at cerberus fossae as long period volcanic quakes. *Journal of Geophysical Research: Planets*, 126(4), e2020JE006518. <https://doi.org/10.1029/2020je006518>
- Khan, A., Ceylan, S., van Driel, M., Giardini, D., Lognonné, P., Samuel, H., et al. (2021). Upper mantle structure of Mars from InSight seismic data. *Science*, 373(6553), 434–438. <https://doi.org/10.1126/science.abf2966>
- Khan, A., van Driel, M., Böse, M., Giardini, D., Ceylan, S., Yan, J., et al. (2016). Single-station and single-event marsquake location and inversion for structure using synthetic Martian waveforms. *Physics of the Earth and Planetary Interiors*, 258, 28–42. <https://doi.org/10.1016/j.pepi.2016.05.017>
- Kim, D., Lekić, V., Irving, J. C., Schmerr, N., Knapmeyer-Endrun, B., Joshi, R., et al. (2021). Improving constraints on planetary interiors with pps receiver functions. *Journal of Geophysical Research: Planets*, 126(11), e2021JE006983. <https://doi.org/10.1029/2021je006983>
- Knapmeyer, M., Oberst, J., Hauber, E., Wählisch, M., Deuchler, C., & Wagner, R. (2006). Working models for spatial distribution and level of Mars' seismicity. *Journal of Geophysical Research*, 111(E11), E11006. <https://doi.org/10.1029/2006JE002708>

- Knapmeyer-Endrun, B., & Kawamura, T. (2020). Nasa's insight mission on Mars—First glimpses of the planet's interior from seismology. *Nature Communications*, 11(1), 1451. <https://doi.org/10.1038/s41467-020-15251-7>
- Knapmeyer-Endrun, B., Panning, M. P., Bissig, F., Joshi, R., Khan, A., Kim, D., et al. (2021). Thickness and structure of the martian crust from InSight seismic data. *Science*, 373(6553), 438–443. <https://doi.org/10.1126/science.abf8966>
- Krischer, L., Megies, T., Barsch, R., Beyreuther, M., Lecocq, T., Caudron, C., & Wassermann, J. (2015). ObsPy: A bridge for seismology into the scientific python ecosystem. *Computational Science & Discovery*, 8(1), 014003. <https://doi.org/10.1088/1749-4699/8/1/014003>
- Langston, C. A. (1979). A single-station fault-plane solution method. *Geophysical Research Letters*, 6(1), 41–44. <https://doi.org/10.1029/gl006i001p00041>
- Lognonné, P., Banerdt, W., Giardini, D., Pike, W., Christensen, U., Laudet, P., et al. (2019). Seis: Insight's seismic experiment for internal structure of Mars. *Space Science Reviews*, 215(1), 12. <https://doi.org/10.1007/s11214-018-0574-6>
- Neumann, G., Zuber, M., Wieczorek, M. A., McGovern, P., Lemoine, F. G., & Smith, D. (2004). Crustal structure of Mars from gravity and topography. *Journal of Geophysical Research*, 109(E8), E08002. <https://doi.org/10.1029/2004je002262>
- Ojo, A. O., Zhao, L., & Wang, X. (2019). Estimations of sensor misorientation for broadband seismic stations in and around Africa. *GeoScience-World*, 90(6), 2188–2204. <https://doi.org/10.1785/0220190103>
- Okal, E. A., & Anderson, D. L. (1978). Theoretical models for Mars and their seismic properties. *Icarus*, 33(3), 514–528. [https://doi.org/10.1016/0019-1035\(78\)90187-2](https://doi.org/10.1016/0019-1035(78)90187-2)
- Olugboji, T. (2020). *Roses 2020: Polarization analysis*. Github. Retrieved from <https://github.com/rosegismo/roses2020>
- Roman, D. C., & Cashman, K. V. (2006). The origin of volcano-tectonic earthquake swarms. *Geology*, 34(6), 457–460. <https://doi.org/10.1130/g22269.1>
- Rubin, A. M. (1992). Dike-induced faulting and graben subsidence in volcanic rift zones. *Journal of Geophysical Research*, 97(B2), 1839–1858. <https://doi.org/10.1029/91jb02170>
- Rubin, A. M. (1995). Propagation of magma-filled cracks. *Annual Review of Earth and Planetary Sciences*, 23(1), 287–336. <https://doi.org/10.1146/annurev.ea.23.050195.001443>
- Schwartz, S. Y. (1995). Source parameters of aftershocks of the 1991 Costa Rica and 1992 Cape Mendocino, California, earthquakes from inversion of local amplitude ratios and broadband waveforms. *Bulletin of the Seismological Society of America*, 85(6), 1560–1575. <https://doi.org/10.1785/bssa0850061560>
- Shang, X., & Tkalcic, H. (2020). Point-source inversion of small and moderate earthquakes from *p*-wave polarities and P/S amplitude ratios within a hierarchical Bayesian framework: Implications for the geysers earthquakes. *Journal of Geophysical Research: Solid Earth*, 125(2), e2019JB018492. <https://doi.org/10.1029/2019JB018492>
- Shelly, D. R., Hill, D. P., Massin, F., Farrell, J., Smith, R. B., & Taira, T. (2013). A fluid-driven earthquake swarm on the margin of the Yellowstone caldera. *Journal of Geophysical Research: Solid Earth*, 118(9), 4872–4886. <https://doi.org/10.1002/jgrb.50362>
- Sita, M. (2022). maddysita/17/Marsquake-SourceCode2022: FAIR compliant repository (Version v1) [Computer software]. Zenodo. <https://doi.org/10.5281/ZENODO.7063492>
- Smith, D., Zuber, M., Neumann, G., Guinness, E., & Slavney, S. (2003). Mars global surveyor laser altimeter mission experiment gridded data record. NASA Planetary Data System. MGS-M-MOLA-5-MEGDR-L3-V1.0.
- Smrekar, S. E., Lognonné, P., Spohn, T., Banerdt, W. B., Breuer, D., Christensen, U., et al. (2018). Pre-mission insights on the interior of Mars. *Space Science Reviews*, 215(1), 3. <https://doi.org/10.1007/s11214-018-0563-9>
- Stein, S., & Wyession, M. (2009). *An introduction to seismology, earthquakes, and earth structure*. John Wiley & Sons.
- Suemoto, Y., Ikeda, T., & Tsuji, T. (2020). Temporal variation and frequency dependence of seismic ambient noise on Mars from polarization analysis. *Geophysical Research Letters*, 47(13), e2020GL087123. <https://doi.org/10.1029/2020GL087123>
- Sun, W., & Tkalcic, H. (2022). Repetitive marsquakes in martian upper mantle. *Nature Communications*, 13(1), 1–9. <https://doi.org/10.1038/s41467-022-29329-x>
- Taylor, J., Teanby, N. A., & Wookey, J. (2013). Estimates of seismic activity in the Cerberus Fossae region of Mars. *Journal of Geophysical Research: Planets*, 118(12), 2570–2581. <https://doi.org/10.1002/2013JE004469>
- The Pandas Development Team. (2021). pandas-dev/pandas: Pandas 1.2.3 (Version v1.2.3) [Computer software]. Zenodo. <https://doi.org/10.5281/ZENODO.4572994>
- USGS. (2021). M 6.2–27 km SSE of Naalehu, Hawaii. Retrieved from <https://earthquake.usgs.gov/earthquakes/eventpage/hv72748782/executive>
- Wessel, P., Luis, J., Uieda, L., Scharroo, R., Wobbe, F., Smith, W. H., & Tian, D. (2019). The generic mapping tools version 6. *Geochemistry, Geophysics, Geosystems*, 20(11), 5556–5564. <https://doi.org/10.1029/2019gc008515>
- Zenhäusern, G., Stähler, S. C., Clinton, J. F., Giardini, D., Ceylan, S., & Garcia, R. F. (2022). Low-frequency marsquakes and where to find them: Back azimuth determination using a polarization analysis approach. *Bulletin of the Seismological Society of America*, 112(4), 1787–1805. <https://doi.org/10.1785/0120220019>
- Zharkov, V. N., & Gudkova, T. V. (2005). Construction of martian interior model. *Solar System Research*, 39(5), 343–373. <https://doi.org/10.1007/s11208-005-0049-7>